UNIVERSITY OF CALIFORNIA
RIVERSIDE

Synthesis and Characterization of Composites with Low-Dimensional Van der Waals Materials

A Thesis submitted in partial satisfaction
of the requirements for the degree of

Master of Science

in

Materials Science and Engineering

by

Lokesh Ramesh

December 2022

Thesis Committee:

Dr. Alexander A. Balandin, Chairperson
Dr. Fariborz Kargar
Dr. Alexander Khitun

The Thesis of Lokesh Ramesh is approved by:

_____

_____

_____

Committee Chairperson

University of California, Riverside

Acknowledgments

I would like to express my sincere gratitude to my Principal Investigator, Dr. Alexander A. Balandin and Dr. Fariborz Kargar, for their supervision and continuous guidance during my work. I am forever thankful to them for sharing their experiences and insights in approaching the problems and ways to solve them.

I would like to thank Sriharsha Sudhindra, for his continuous support and guidance throughout the research. I would like to thank all the current and previous lab mates for their motivation and encouragement whenever I felt down and for being there and providing advice and support towards my work. I would also like to thank Dr. Subhajit Ghosh, Dr. Zahra Barani Beiranvand, Erick Guzman, Dylan Wright, Maedeh Taheri, and Jonas Brown for their encouragement and for teaching me about composite preparation, device fabrication, SEM, Raman, and Brillouin spectroscopy. I am honored to thank my colleague and my friend Tekwam Geremew for being supportive and helping me throughout my work. I would like to thank Zahra Ebrahimmalekshah Nataj for helping me in measuring Raman for my work. I would also like to thank Dr. Saba Baraghani for training me in the printer system.

I would like to express my gratitude to our collaborator from the University of Georgia, Professor Tina T. Salguero, and her team for helping us with the synthesis of materials.

I would like to thank the University of California – Riverside, Department of Materials Science and Engineering, and Department of Electrical and Computer Engineering, for giving me the wonderful lifetime opportunity to be a part of this institution.

And finally, I take this moment to thank my parents for their sacrifices, support, and trust in me.

ABSTRACT OF THE THESIS

Synthesis and Characterization of Composites with Low-Dimensional Van der Waals Materials

by

Lokesh Ramesh

Master of Science, Department of Materials Science and Engineering
University of California, Riverside, December 2022
Dr. Alexander A. Balandin, Chairperson

This thesis reports on the synthesis of polymer composites with fillers comprised of low-dimensional van der Waals materials. The quasi-one-dimensional (1D) van der Waals materials are characterized by the 1D motifs in their crystal structure. The research was focused on NbS_3 – a material that can form numerous polytypes. The fillers for the composites were prepared by the liquid-phase exfoliation of the small crystals into needle-like ribbons with nm-scale thickness and μm-scale length. The exfoliated NbS_3 fillers were dispersed in the solvents to produce composites. The speed mixing and sonication processes were used to control the filler sizes. The resulting composite materials were characterized using Raman light-scattering spectroscopy, differential scanning calorimetry, thermal diffusivity, and thermal conductivity measurements. The characterization data indicate that the NbS_3 fillers preserved their intrinsic properties. The

results of the thesis research confirm that low-dimensional van der Waals materials are suitable for composite preparation. The obtained results can be used for the development of inks for printed electronics and multi-functional composites.

Table of Contents

List of Figures

List of Tables

Chapter 1 Introduction and Motivations

1.1 Motivations

The increasing demand for realizing flexible electronics and deformable form factors over large areas was challenging and limits their production with conventional micro/nanofabrication manufacturing techniques. Developing new fabrication methods which are necessary for developing flexible electronics while striving to achieve cost-effective large-scale production needed. Printed electronic technologies emerge as an alternative [1–5]. The research on printed electronics has created attention, due to its high throughput production of flexible printed electronic devices with lower cost and processing requirements [6,7]. It reduces the operational complexity, and chemical waste during production, and also they offer low processing temperature and faster development. There are similarities in the synthesis of inks for inkjet printers and polymer composites. Understanding polymer composites can provide valuable information for future use in inkjet-printed electronics.

Polymer composites have various engineering applications including in the semiconductor industry, automobile, and space industries. The use of these polymer composites has become a state-of-the-art technology. The distribution of nanoparticles in a polymer matrix forms a nanocomposite. The maximum quantity of fibers that could be fitted in the polymer matrix is about 70 vol.%. In nanotechnology, a reduction in the size of the particle increases the surface area in the polymer, many nanofillers in the matrix,

and very less distance between them. The nanoparticles like CNT act as reinforcement elements to improve the mechanical and/or electrical properties. This could be achieved when the interaction between the nanoparticles and the matrix polymer (epoxy) is sufficiently good. It is necessary to introduce new dispersion techniques. This is crucial for the CNT– epoxy matrix interaction, by breaking up the intermolecular bonds, leading to the formation of agglomerates. It is recommended to operate the high-speed mixer at low speed, to reduce the effect. With this situation in respect, a promising solution to prevent agglomeration is to sonicate the CNT with an appropriate solvent (acetone). The solvent is evaporated by heating and then mixed with an epoxy matrix [8].

A traditional way to improve the properties of polymeric materials is by dispersing the glass, carbon or kevlar fibers, or ceramic particles to the matrix, to determine the suitable composite [9]. There are a few disadvantages of these fillers such as reduction in strain to failure, impact strength, and fracture toughness, which is due to the diameters of these reinforcements in the micrometers range. A promising approach to overcome this problem is by reducing the diameters to several nanometers. The resulting nanocomposites will have more remarkable properties than pristine polymer matrices. The surrounding polymer matrix will be in contact with many nanoparticles with high surface area, then the resulting nanocomposite may have interfacial-determined behavior. TiO_2 particles were mixed with epoxy resin at a low shear rate, by a laboratory propeller. The SEM image proved a visible agglomeration of nanoparticles that are not fully dispersed. The application of ultrasound further improved the combination by the breakage of agglomerates. The

combination of mechanical stirring and ultrasound waves was able to disperse CNT into epoxy resin [10].

The hybrid composites are derived from two components with synergistic properties. The advantages of nanoparticles include efficient reinforcements with minimal loss of heat stability, ductility, improved abrasion resistance, better gas permeability, and reduced shrinkage, with altered electronic and optical properties. The decrease in the size of reinforcement to the nano range enables good optical transparency. The polymer nanocomposites open up a new perspective for optical materials as the size of the particles is less than the wavelength of light, making them suitable for the optoelectronic field [11].

The polymers can be classified into thermoplastics and thermosetting plastics. The most used thermoplastics are polypropylene (PP), polyethylene, and polyvinyl chloride (PVC), while thermosetting plastics include phenolic, epoxy, and polyester resins [12]. A rapid increase in worldwide demand for nanocomposites due to their superior electrical, thermal, optical, and other properties in packaging, electrical, automotive, and other applications. The global nanocomposite market records a volume of sales of over 80%, dominated by the US and Europe in 2008. Increased R&D activities have been carried out by research institutions and industries to explore efficient methods for developing low-cost nanocomposites in large volumes. Nanocomposite thermosets enhance the reinforcement property of polyesters and epoxy compounds. However, it was predicted that by 2025, nanotube-based composites will gain a sizable portion of the market, replacing other conductive materials, in electrical and electronic applications. It is found that the thermal

stability of the polymer composites was improved by mixing nanocarbon materials such as CNTs and graphene [13].

Table 1.1: Representation of demand for nanocomposites in the US (million pounds) [13]

	2005	2010	2020
Nanocomposite demand	154	344	7030
Thermoplastics	152	329	5600
Thermosets	2	15	1430

The high thermal interface resistance at a thermal junction of the material in the presence of heat flux, causes significant temperature discontinuity, due to the miniaturization of devices and/or high-power usage. The components with poor thermal interface remaining at high temperatures and not cooled down could deteriorate the reliability, performance, and lifetime of the components. The need to improve the heat conduction of the device at the thermal junction, motivated the development of thermal interface materials (TIMs), by filling them at surface irregularities. These thermally conductive, low thermal resistance materials achieved better thermal management and mechanical properties [14–16].

The van der Waals materials are strongly bonded in the two-dimensional plane, but with weak dispersion forces in the third dimension. Graphite is the most used vdW material in electrodes, lubricants, fibers, heat exchangers, and batteries. A single two-dimensional

layer of graphite, known as graphene, introduced a new path in quasi-2D materials that have tunable thickness and electronic bandgap, as well as confinement effects [17].

Due to the lack of an electronic bandgap in graphene, its discovery also led the way to the study of other 2D layered materials with semiconducting behavior. The other materials include transition metal dichalcogenides (TMDs) and transition metal trichalcogenides (TMTs), which are semiconductor materials of the type MX_2 and MX_3, where M is a transition metal atom and X is a chalcogen atom [18]. These layered materials include conductors (graphene), semi-conductors (MoS_2, WSe_2) with varying bandgaps and insulators such as boron nitride (BN). Since the interactions between adjacent layers of two-dimensional layered materials are characterized by the van der Waals force, this provides freedom to integrate disparate materials without the constraints of crystal lattice matching, to produce diverse van der Waals heterostructures [19].

1.2 Quasi-2D Materials

The layered quasi-two-dimensional (2D) van der Waals (vdW) materials, such as graphene, hexagonal boron nitride, transition metal dichalcogenides (TMDs), including MoS_2, $MoSe_2$, 1T-TaS_2, and WS_2 were studied previously [20–23]. These vdW materials were promising for printing due to easier ink development methods, and the weaker vdW bonding between the layers allows exfoliation into flexible quasi-2D layers. The liquid-phase exfoliation process is utilized to produce flakes from the crystal which are dispersed in proper solvents. TMDs increase the functionality of the inks as they exhibit tunable electronic and mechanical properties.

The one serious issue with using 2D material inks in printed electronics is that the intrinsic properties of semiconducting materials are compromised by electron hopping mechanisms [24–26]. A printed layer of vdW ink with semiconducting fillers does not offer the electrical conductivity of the true conduction band semiconductor. For instance, the electrical conductivity of MoS_2 will be of a hopping type of mechanism, that has intrinsic semiconducting properties of 2D material. This gives the reason why electron mobilities in most transistors are below 10 $cm^2V^{-1}s^{-1}$ and in many cases are below 0.5 $\mathrm{cm^2V^{-1}s^{-1}}$. Some extra processing steps have been included in nanoparticle ink to achieve mobility above 10 $\mathrm{cm^2V^{-1}s^{-1}}$ [27,28]. However, band-type conduction is not attained, leading to the limitation of electron transport by the interface between the two contacting fillers. This effect has been overcome by the CDW materials which are not limited by the interface between the percolating fillers, discussed further.

1.3 Quasi-1D Materials

In a recent trend, transition metal trichalcogenides are being focused on as their quasi-1D properties originate from a reduced in-plane structural symmetry, which is interesting compared to dichalcogenides (TMDs). This character gives group IV-V transition metal trichalcogenides class of materials with strong anisotropies in the electrical and optical properties [29,30]. The quasi-1D crystals are stronger along the atomic chain by a covalent bond and weak van der Waals bond along the perpendicular direction to the chains [31–33]. Transition metal trichalcogenides (TMTs) are a prominent group of quasi-1D vdW materials, where *M* is a transition metal and *X* is a chalcogen. TiS_3, $TaSe_3$, NbS_3, ZrS_3, and $ZrTe_3$ are a few example materials of this group [34–36]. Unlike TMDs on exfoliation forms into quasi-2D atomic planes, TMT crystals transform into quasi-1D structures with high aspect ratios [37].

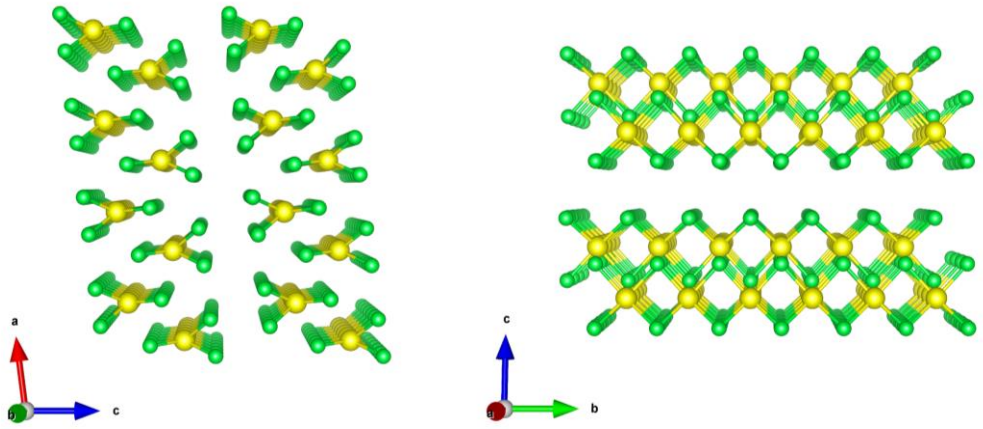

Fig. 1.1: Crystal structure of NbS_3 Polymorph-V.

The feasibility of the use of such materials in the inks for printed devices is based on the most recent developments in quasi-1D materials synthesis and exfoliation. These exfoliated bundles of quasi-1D atomic chains offer specific advantages due to their high aspect ratio and flexibility, such as smaller loading fractions required to achieve electrical conduction, better connectivity of the individual flakes, and more narrowly printed lines [38,39]. This led to exploring the material with other state-of-the-art applications including composites with polymers. Fig. 1.1 shows the single-layer crystal structure of NbS_3 used in this project.

In this work, the thermal characterization and Raman characterization of the bulk crystal and exfoliated fillers were discussed. The steps to exfoliate the crystal and to reduce them to fillers are explained. The procedure to make composites using epoxy resin and PVDF was discussed, along with the procedure to make composite inks. The theory of instruments used such as Differential Scanning Calorimetry, and Laser Flash Analysis was discussed. The preparation methods and required properties of the ink are discussed. Also, the future application of the ink could be used as the channel in nanodevices, which could be one of the future applications that were explained as well.

Chapter 2 Material Synthesis and Experimental Techniques

2.1 Crystal Synthesis

The quasi-one-dimensional NbS_3 crystal used in this study as shown in Fig. 2.1 was synthesized by the direct reaction by the chemical vapor transport method. The highly pure Nb (4 N, 2.4565 g) and S (4 N, 2.55 g) were mixed in the molar ratio of 1:3.1 with a 10% excess of sulfur. Then, they are loaded into the flame-sealed silica tube, containing the charge at the pressure of 10^{-4} Torr.

Fig. 2.1: NbS_3 material synthesized by CVT method. The bulk crystal material was provided by the collaborators at the University of Georgia.

The tube was then placed in the two-zone furnace, one being the source zone and the other being the growth zone fixed at 700 °C and 600 °C, respectively. The furnace is turned on for two weeks, giving sufficient period for the crystal growth, and then turned off. The growth continued for two weeks in a sealed quartz tube. The growth takes place at a temperature in the range between 600-800 °C and the temperature gradient varies

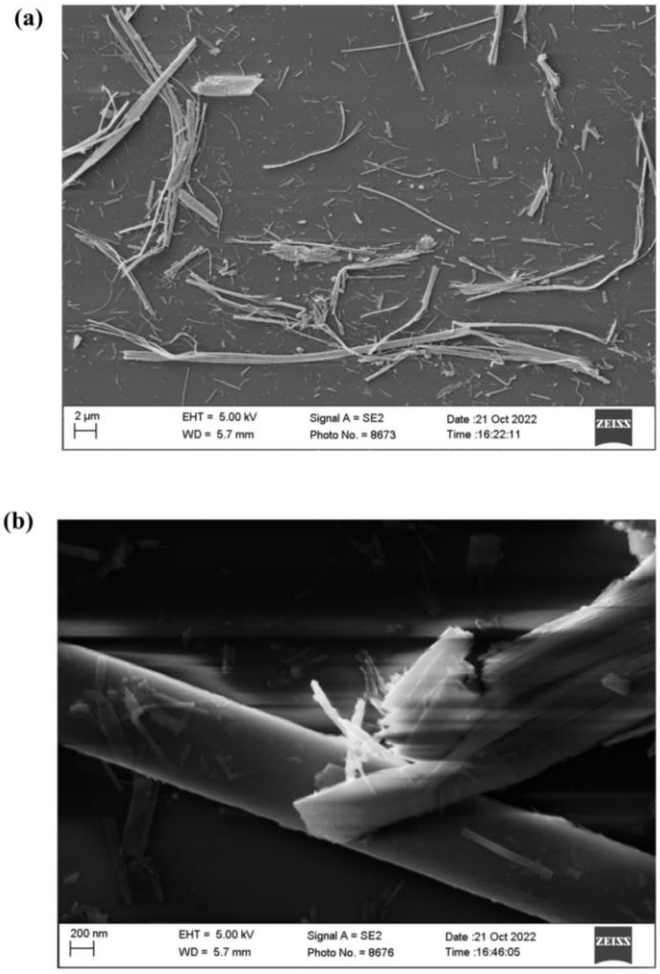

Fig. 2.2: SEM images of NbS_3 threads that are mechanically exfoliated (scale bar 20 µm and 200 nm).

between 1-2.5 °C/cm. Phase II exhibits two Peierls transitions at T = 360 K and T = 150 K. The transition at 150 K tends to vanish for thinner samples (10^{-3}– 10^{-2} μm^2) [40].

2.2 Preparation of Composites

2.2.1 Study of Solvents

To make composites of quasi-1D materials, suitable polymer solvents must be selected. In this work, a few polymer solvents were studied such as epoxy resin, polyethylene glycol, polyethylene oxide, polyvinyl alcohol, polyvinyl fluoride, lithium perchlorate, poly diallyl dimethyl ammonium chloride, sodium cholate hydrate, poly sodium 4-styrene sulfonate, and suitable polymers were chosen. Epoxy resin has been used as a common polymer in making composites and shows excellent chemical resistance and strength properties [41,42]. Polyethylene glycol and polyethylene oxide melt at 70 °C and had a glass transition at 66 °C and -50 °C respectively, as the phase transition temperature of NbS_3 was 80 °C, so these polymers cannot be selected [43–47]. Polyvinyl alcohol has a glass transition temperature at 80 °C which is like NbS_3, and the polymer starts to discolorize, which leads to a search for different polymers [48].

Lithium perchlorate has been used in the application of electrolytes in lithium-ion battery devices, also has a glass transition temperature between -10 °C to 64 °C, which again cannot be used as the polymer [49,50]. Sodium cholate hydrate has been used majorly in the surfactant exfoliation process and poly sodium 4-styrene sulfonate has been used as a dispersing agent [51,52]. Polyvinylidene fluoride has been used as a polymer for making

composites and has been in EMI shielding applications [53–55]. So, this PVDF and epoxy resin has been used as polymers to prepare composites.

2.2.2 Liquid Phase Exfoliation

The NbS_3 crystal which is synthesized using the CVT method was exfoliated in the ethanol and DI water solvent mixture. The model of the ultra-bath sonicator used in this work is Branson 5510 as shown in Fig. 2.3. The Ethanol and DI water are mixed in a ratio of 1:1. Approximately 25 mg of the bulk crystals were placed in a vial containing 20 ml of the solvents. The mixture was sonicated in an ultrasonic bath Sonicator for 12 hours as in Fig 2.4 (a).

Fig. 2.3: Image of Branson 5510 ultra-bath sonicator.

The exfoliation of the crystals was checked. Any unexfoliated crystals found at the end of the exfoliation were processed to exfoliation for another 90 minutes until exfoliated. Finally, the solution was dried out for at least 8–12 hours. This step is necessary to remove

all the solvents that are present along with the NbS_3 fillers. Then the exfoliated van der Waals materials are extracted from the dishes and stored for further experimentation as shown in Fig. 2.4 (b).

2.2.3 Preparation of the Polymer-Based Composites

The selection of a suitable polymer is the most important step in preparing the composite samples as it will be influencing the shape, size, and roughness factors. From the study of the solvents section, it is concluded that polyvinylidene fluoride (PVDF) and epoxy resin are suitable polymers for this application. To prepare the base solvent for the composite, PVDF powder is added to Dimethylformamide solvent (DMF), in a beaker. The PVDF powder and DMF in the beaker are then placed over the hot plate to facilitate the mixing process. A magnetic stirrer is placed in the beaker to improve the homogeneous mixing of the solvent. The speed of the stir is set between 250-300 rpm, which is more suitable for mixing PVDF with DMF.

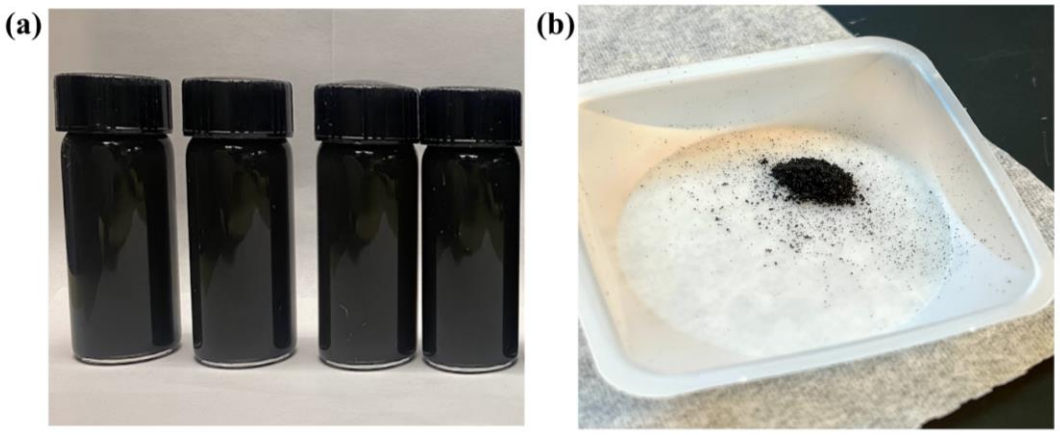

Fig. 2.4: (a) Exfoliated NbS_3 material in ethanol and DI water solvent (b) Solvent-free dried NbS_3 fillers.

Along with mixing and simultaneous heating of the polymer and the solvent, the desired mixture could be achieved. The desired viscosity is achieved by keeping the beaker in the open position, without covering the top, so that the DMF could evaporate. By controlling the amount of evaporation of the DMF from the mixture, the desired viscous mixture is achieved as per the requirement for making the composite. In this work, the viscosity is chosen based on the density of the NbS_3. A specific amount of 0.85 g of PVDF solvent was chosen to make a pristine PVDF sample.

Fig. 2.5: Image of a speed mixer used in this project.

The solvent is poured on the glass petri dish and the solvent is spread over the dish homogeneously. The dish is then placed on the hot plate to dry the PVDF solvent. In approximately, after two hours, the PVDF solvent will be dried out. A thin film of pristine PVDF is formed. This film could be removed from the dish using tweezers, by scrapping

them in the corner and slowly peeling it from the surface. The film is then cut into the required size as per the LFAs sample size requirement.

For making a composite with NbS_3, 26.3 mg of exfoliated NbS3 filler is taken and stored in a small container, suitable for the shear mixer as shown in Fig. 2.5. 0.85 g of PVDF solution is then added to the fillers. The container is then placed in the shear mixer and turned on. The solution is mixed at the lowest speed possible at 320 rpm for 5 min using the Speed Mixer. The mixing speed and time must be minimized to avoid the agglomeration of the fillers in the solution. This step will support the process of a homogeneous mixture. As the next step, it is poured on a smooth and clean surface and is allowed to dry. After sufficient time for drying around 2 hours, a thin film of NbS_3 loaded PVDF thin film composite is developed. Similarly, a different weight of 44.7 mg of fillers has been added to the same 0.85 g of the PVDF solvent to prepare a composite of different filler loadings as shown in Fig. 2.6.

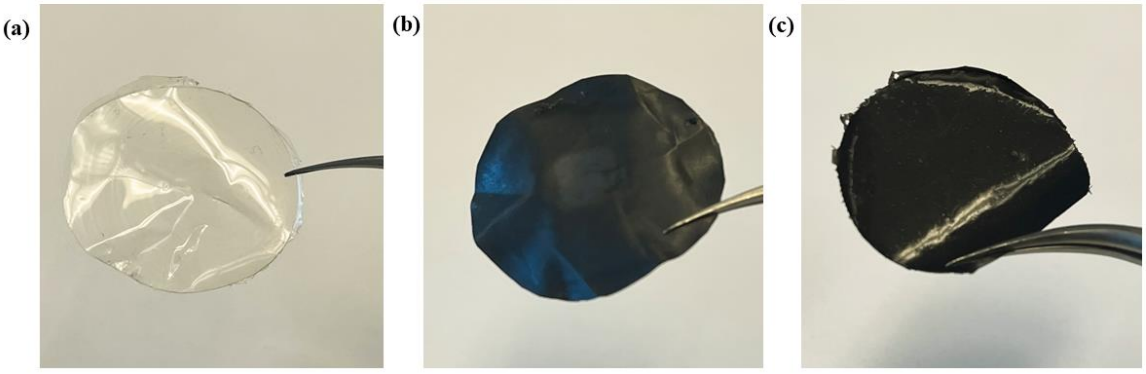

Fig. 2.6: PVDF composites with exfoliated NbS_3 fillers (a) pristine PVDF (b) 2.2 vol.% (c) 4.7 vol.%.

Epoxy resin is the most common polymer which is being used to make composites. To prepare the base polymer for the composite, epoxy resin is taken in a small container, like the process for making PVDF composite. The hardener is also poured into the small container. The mixture of epoxy and hardener is made at a ratio of 100:12. Now, 2 g of epoxy resin is taken, and 0.24 g of hardener is poured into the container. The mixture in the small container is then placed in the shear mixer for mixing. The solution is mixed at the lowest speed of 320 rpm for 15 min using the speed mixer. The mixture is then kept under a vacuum pump for 20 min, to remove the air bubbles that are formed during the mixing of the resin and hardener.

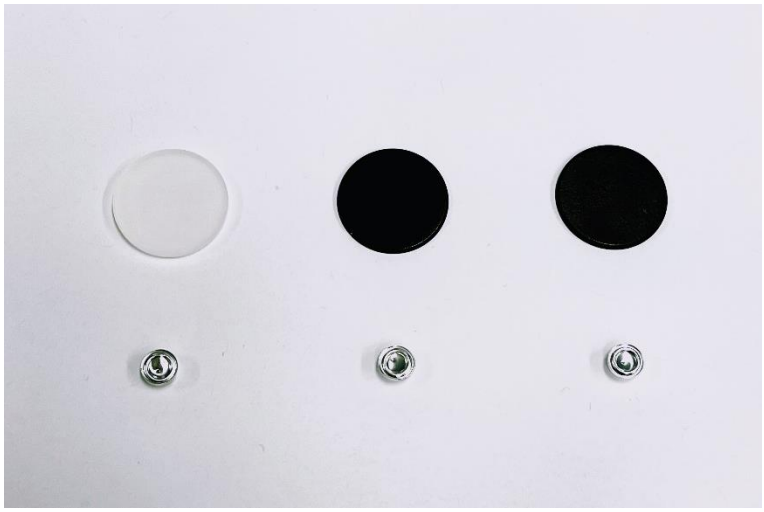

Fig. 2.7: Epoxy composites with exfoliated NbS_3 fillers (a) pristine epoxy (b) 1.42 vol.% (c) 2.5 vol.%. Aluminum crucibles were prepared for DSC measurements.

Next, the mixed polymer is poured into a clean silicon mold the size of 1 inch. The mixture is set to cure for 16 hours, to get a pristine epoxy sample. After the sample is completely cured, it is then polished with the Allied polisher to get a similar thickness

across the sample. The epoxy mixture of 2.24 g is taken in a container and 105.5 mg of NbS_3 filler is added to the container. It is then mixed with the shear mixer. The container is closed tightly and then placed in the holder of the mixer. The lowest possible speed is maintained to avoid the agglomeration and the homogeneous mixture at 320 rpm for 15 min, like the preparation method of PVDF composite. The mixture is then kept under a vacuum for 20 min to remove all the air bubbles, which were formed during mixing. Now, similar to the pristine epoxy preparation method, the mixture is poured into the silicon mold and dried for 16 hours, and polished to homogenous thickness all across the sample. Similarly, different weight percentages of the fillers have been added to the same 2.24 g of the epoxy to prepare a composite with different filler loadings as shown in Fig. 2.7.

Chapter 3 Results and Discussion

3.1 Specific Heat Capacity Measurements

The most important quantity in differential scanning calorimetry is the temperature, as it is the only measured quantity. The other quantities including specific heat, thermal conductivity, entropy, enthalpy, heat flow, etc., were calculated from the temperature changes, between the sample and reference temperature. Heat is a form of energy that flows from a higher-temperature body to a lower-temperature body, causing an exchange of energy between the two thermodynamic systems. Apart from the three major forms of heat flow, latent heat or heat of transition is equally important during the phase transition of the material. The latent heat also known as the heat of transition, is defined as the amount of heat absorbed or emitted by a material during phase transition, at which the temperature of the body remains constant, but the absorption or emission of hidden heat. Specific heat is the amount of energy required to increase the temperature of one gram of the material by one Celsius degree. The sample material is heated as a function of linear temperature, where the heat flow through the material is directly proportional to the specific heat of the sample. The heat capacity is measured by using the equation [56],

$$C_{ps} = \left({}^{H}/_{h}\right)\left({}^{m_r}/_{m_s}\right)C_{pr} \tag{3.1}$$

where $C_{ps,}$ unknown heat capacity of the sample (J/gK); H, the difference between sample and baseline (K); h, *the* difference between the reference and baseline (K); m_r, the mass of

the reference (g); m_s, the mass of the test sample (g) and C_{pr}, the heat capacity of the reference (J/gK).

Fig. 3.1: DSC 214 Polyma system.

The term thermodynamic phase transition is defined as the change from one phase to another phase in a thermodynamic system because of a change in temperature and/or pressure. The first-order phase transition occurs when a first partial derivative of free energy exhibits discontinuity with a thermodynamic variable such as temperature, and pressure. These derivatives are the volume, enthalpy, and entropy, caused by first-order transitions such as melting, evaporation, sublimation, condensation, deposition, and crystallization. The second-order phase transition occurs when the above-mentioned first-order transition is continuous, but the second partial derivative of free energy is

discontinuous. It includes magnetic transition at the Curie point, the super-fluid transition of liquid helium, and the glass transition of polymers.

The glass transition temperature is the temperature where the glassy state of the polymer changes into a rubbery or molten state, resembling a second-order thermodynamic transition, exhibiting a heat capacity jump. This transition temperature is usually defined as the temperature at the half-height of the heat capacity increase, also known as the temperature of half-unfreezing ($\frac{1}{2}\Delta C_p$). The heating rate of both sample and reference in power consumption DSC is expressed as,

$$T_{av} = (T_r + T_s)/2 \tag{3.2}$$

Where T_{av}, average temperature (K); T_r, reference temperature (K) and T_s, sample temperature (K). The temperature of the sample and reference returned from the sensors is compared to the programmed temperature, as the temperature with the sample is heat slower than the reference. The temperature difference is detected and adjusted based on the feedback from the differential temperature amplifier.

The heat flux DSC is another type of instrument, that operates based on the thermal equivalent of Ohm's law,

$$Q = \Delta T / R \tag{3.3}$$

Where Q, is the heat flow rate (Js^{-1}); ΔT, is the temperature difference between the reference and sample sensor (K), and R, is the thermal resistance of the heat leak disk (K/Js^{-1}). The heating block with the sensors from the reference and sample holder and the furnace

is responsible to maintain a constant temperature inside the chamber and maintaining heating and as well as cooling at a linear rate. The resolution and sensitivity of the measurements could also be improved based on the heating rate and mass of the sample. A slow heating rate must be considered to get high resolution, but this takes more time to perform, whereas the sensitivity can be improved by increasing the mass of the sample. The range of the sample mass used in DSC lies between 3 and 10 mg. The standard DSC crucible used in our measurements is made of aluminum and includes a pan and a punch-holed lid.

As it is often impossible to maintain the solid and liquid polymer samples at a constant volume when the temperature changes, it is impossible to measure the C_v, Thus leaving the DSC to measure the C_p of polymers. So, the DSC signal is closely proportional to the heat capacity of the sample, [56,57] where C_p is heat capacity at constant pressure and C_v is heat capacity at constant volume.

The interpretation of DSC curves plays a crucial role in determining the property of the sample. Sometimes due to external or internal disturbances, different first-order and second-order peaks will be observed. The possible reason for those peaks and curves includes polymer material not being pressed against the base of the pan, samples with irregular shapes, a slight shift of the pan from the disk, mechanical vibration/shock around the sensor, sudden change in room temperature, intermittent closing of the lid of the pan due to condensation of the sample or samples that produce foam, contamination on the surface the sensor or on the bottom of the pan, discharge of static electricity in a metallic part of the system, and the burst of the lid of the pan due to increased vapor pressure. The

other transitions include the result of weight loss due to evaporation, curie transition, chemical reaction, glass transition, and solid-solid transitions [58].

The Differential Scanning Calorimetry (DSC) system contains two sample holders, with one on the left reference material and the right will be sample material. Initially, the specific heat will be measured with two empty aluminum crucibles to establish the baseline. This step is performed to determine the differential losses or fluctuations between two samples, caused by the temperature mismatch. After the measurement ends, the reference material with already known specific heat values is measured. Then reference is replaced with the unknown sample material and heat flow is measured [59].

In this work, DSC 214 Polyma by Netzsch Instruments is utilized to measure heat flow and specific heat values of the NbS_3 polymorphs as shown in Fig. 3.1. The Aluminum crucible of 5mm diameter along with the lid is used to enclose the sample materials to be measured. The heating and cooling rate is kept at 20 K/min, which is an ideal rate to reduce the measurement timing along with the sharper measurements. The reference sample in this work is taken from Al_2O_3.

The recommended minimum weight of the sample must be above 10 mg and must be maintained for all samples. The mass of the test samples includes NbS_3 Polymorph V crystal, exfoliated NbS_3 fillers, and composites made of PVDF with NbS_3 at different fraction loadings were measured. The measurements were carried out over days due to sample preparation limitations as discussed in the Sample Preparation chapter. Fig. 3.2 (a) shows the baseline and NbS_3 crystals measurements along with Al_2O_3.

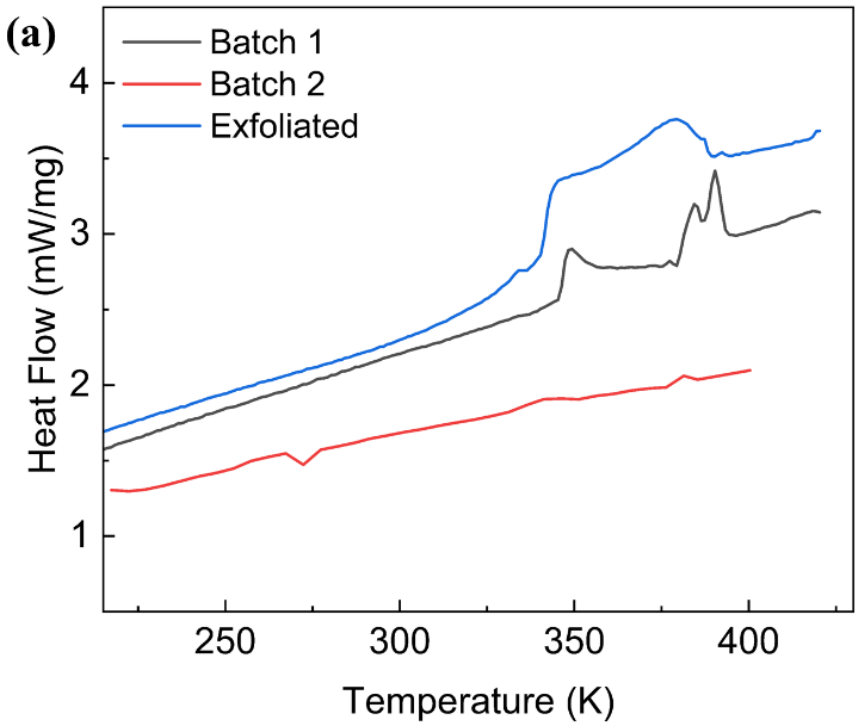

Fig. 3.2 (a): Heat flow signals of NbS_3 crystal of two different batches and exfoliated nanowire.

The measurement of heat flow through the NbS_3 Polymorph V samples is to determine the phase transition that occurs at the phase transition temperatures. The epoxy polymer is measured to show that the transition is not due to the polymer that we are using. The change in the curve at 335 K is due to the glass transition temperature of the epoxy which is used in this work. It is found that the current polymorph has charge density waves transported at phase transition temperatures between 330 K and 370 K. The peaks that could be seen at temperatures over the expected range are due to the presence of different other polymorphs in polymorph-V as shown in Fig. 3.2 (a). The heat flow signal of Batch 1 and its exfoliated crystal clearly shows the presence of other polymorphs. The heat flow

signal of batch 2 showing an odd peak at room temperature at 275 K is due to an error in the baseline.

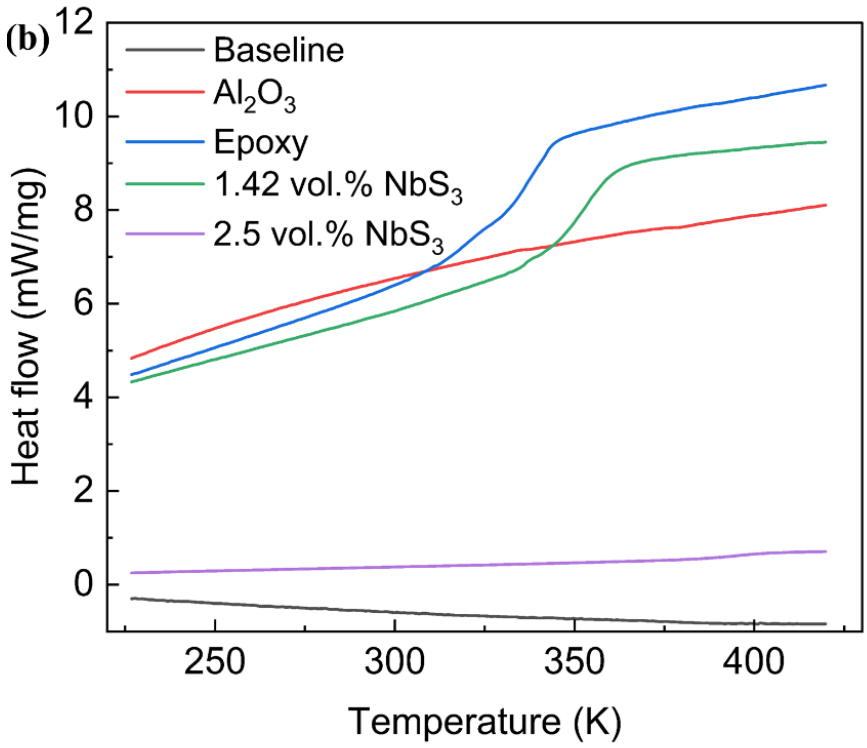

Fig. 3.2 (b): Heat flow signals of epoxy composites with NbS_3 fillers.

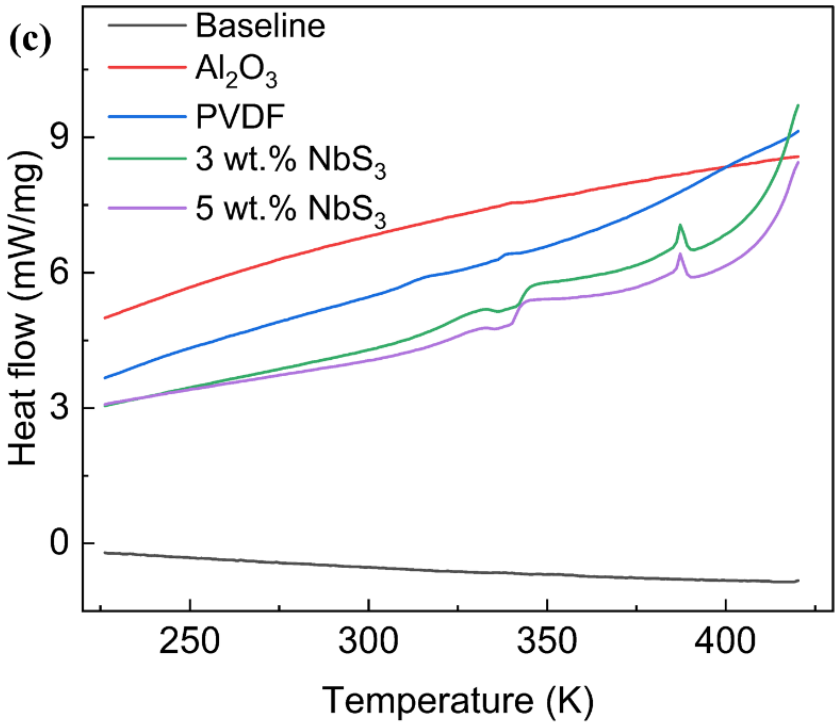

Fig. 3.2 (c): Heat flow signals of PVDF composites with NbS_3 fillers.

The epoxy composites showed transition at 375 K during their first trials of both samples, while the pristine sample does not show any phase transition. But this result was not reproducible after the first trial. As shown in Fig. 3.2 (b), the results of the samples made with epoxy couldn't exhibit the phase transition due to its glass transition temperature at 60-100 ^{o}C. The composites made with PVDF along NbS_3 filler at 3 wt.% and 5 wt.% represent the phase transition temperature in the same range as shown in Fig. 3.2 (c). A different batch of PVDF composites was used to measure them with the LFA, due to the porosity in these samples. The specific heat capacity of all the samples was extracted using Al_2O_3 heat flow signals, by using the C_p ratio method. The extracted specific heat capacity data were plotted as shown in Fig. 3.3.

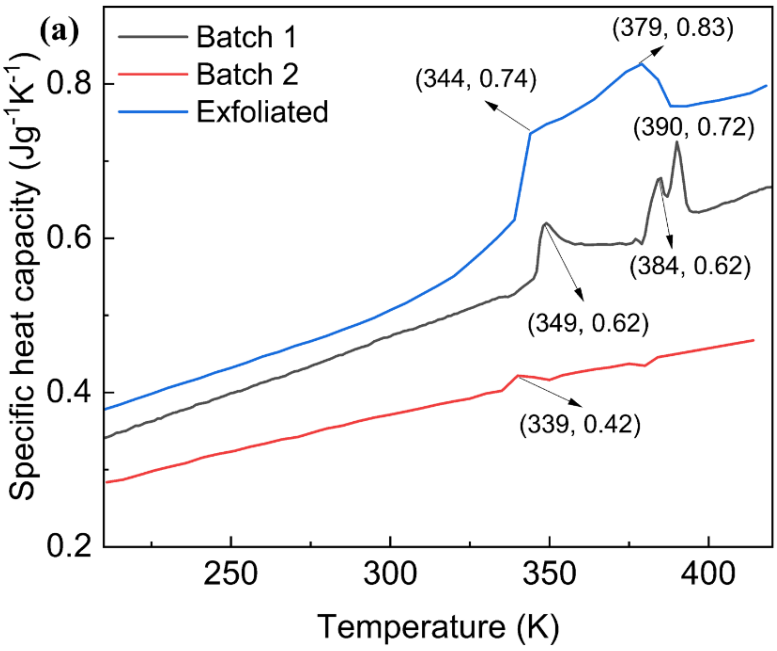

Fig. 3.3 (a): Specific heat capacity of NbS_3 crystal of two different batches along with exfoliated nanowire show phase transition around 350 K and 385 K.

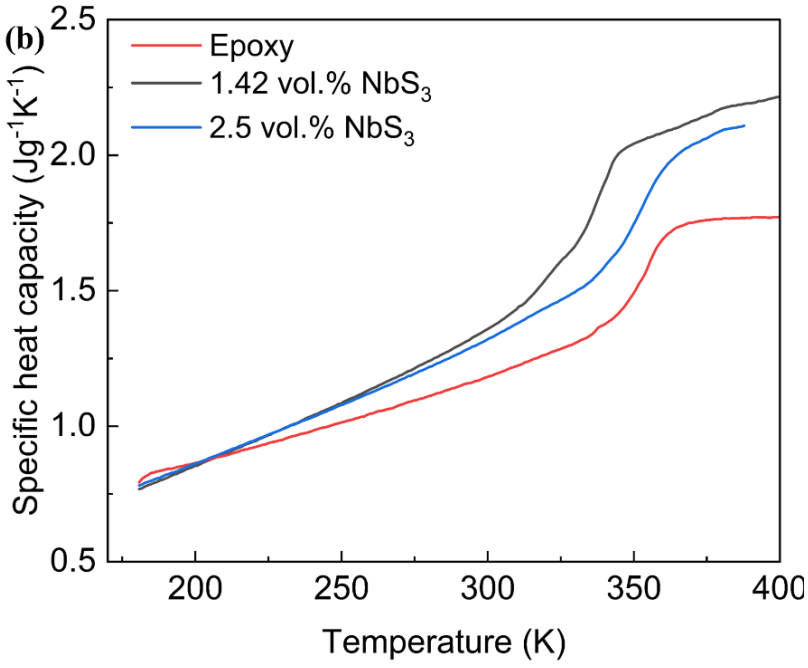

Fig. 3.3 (b): Specific heat capacity of epoxy composites with NbS_3 fillers at two different weight loadings.

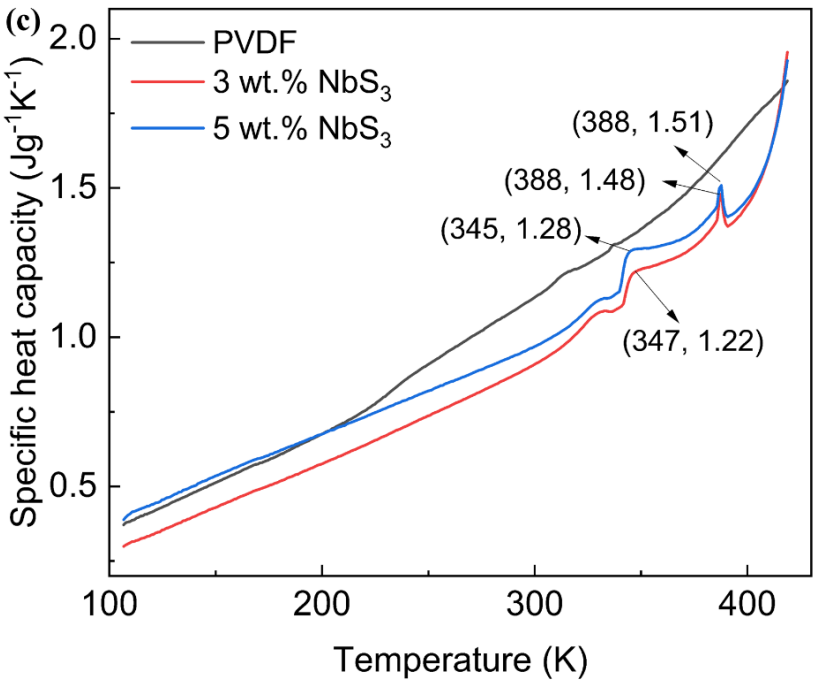

Fig. 3.3 (c): Specific heat capacity of PVDF composites with NbS_3 fillers at two different weight loadings.

3.2 Thermal Diffusivity Measurements

The thermophysical properties of polymers play a critical role in their performance in high-temperature applications. Thermal diffusivity and thermal conductivity are the properties that define the transfer of heat through the materials. Applications that require maximized heat flow in the materials, should choose high thermal conductivity materials, whereas low thermal conductivity materials are chosen to reduce the dissipation of the heat.

Fig. 3.4: LFA 467 Hyper-Flash system used in this project.

Thermal diffusivity is the rate of transfer of heat waves when there is a temperature change in the material. The equation relating specific heat, thermal conductivity, and

thermal diffusivity is related in an equation by

$$\propto = \frac{k}{\rho\, C_p} \tag{3.2}$$

$\propto$, thermal diffusivity (mm^2/s); k , thermal conductivity (W/mK); ρ , bulk density (kg/m^3) and C_p, specific heat capacity (J/gK) [60].

In this work, LFA 467 HyperFlash by Netzsch Instruments is utilized to measure thermal diffusivity and thermal conductivity values of the NbS_3 composites as shown in Fig. 3.4. The temperature range is set to be from room temperature to 423 K. The reference material standard dimension is 1-inch diameter and the sample materials diameter for epoxy composites is 1 inch and for PVDF composites, the sample diameter is 6 mm. The reference sample in this work is taken pyrocerum, of diameter 1 inch, which is used to extract the thermal conductivity of the samples.

The temperature step rate is 10 K for both epoxy and PVDF composites. The thickness of all the samples is not the same, this is due to variations in the filler loading in the polymers. But, since the density and thickness of the samples are required to determine the thermal conductivity, the values of those are measured using the vernier caliper and weight scale. It is evident from Fig. 3.5, that increase in filler loading decreases the thermal diffusivities through the epoxy composites, which is because of the increased number of NbS_3 fillers present inside the composites. These fillers show resistance to the heat that is being flashed from the source of the instrument. The pristine PVDF shows lesser diffusivity, but in composites, the lesser filler content shows high diffusivity than higher volume loading, this could be due to filler agglomeration at one corner or due to the density

of fillers that settles randomly. Also, an increase in filler loading increases the specific heat capacity of the polymer due to the inclusion of NbS_3 fillers.

The unusual behavior of epoxy composites in LFA measurements is due to the following possible reasons such as, not using the exact ratio of epoxy resin and hardener as curing requires an exact ratio to start the chemical reaction, not mixing the resin and hardener thoroughly, and also after adding fillers, or the composites weren't cured completely, at room temperature, which could be avoided by curing the samples at elevated temperatures, around 60 ^{o}C.

The thermal diffusivity values are exported by using the Analysis software. The thermal diffusivity plots for both epoxy and PVDF composites determined could be seen in Fig. 3.6.

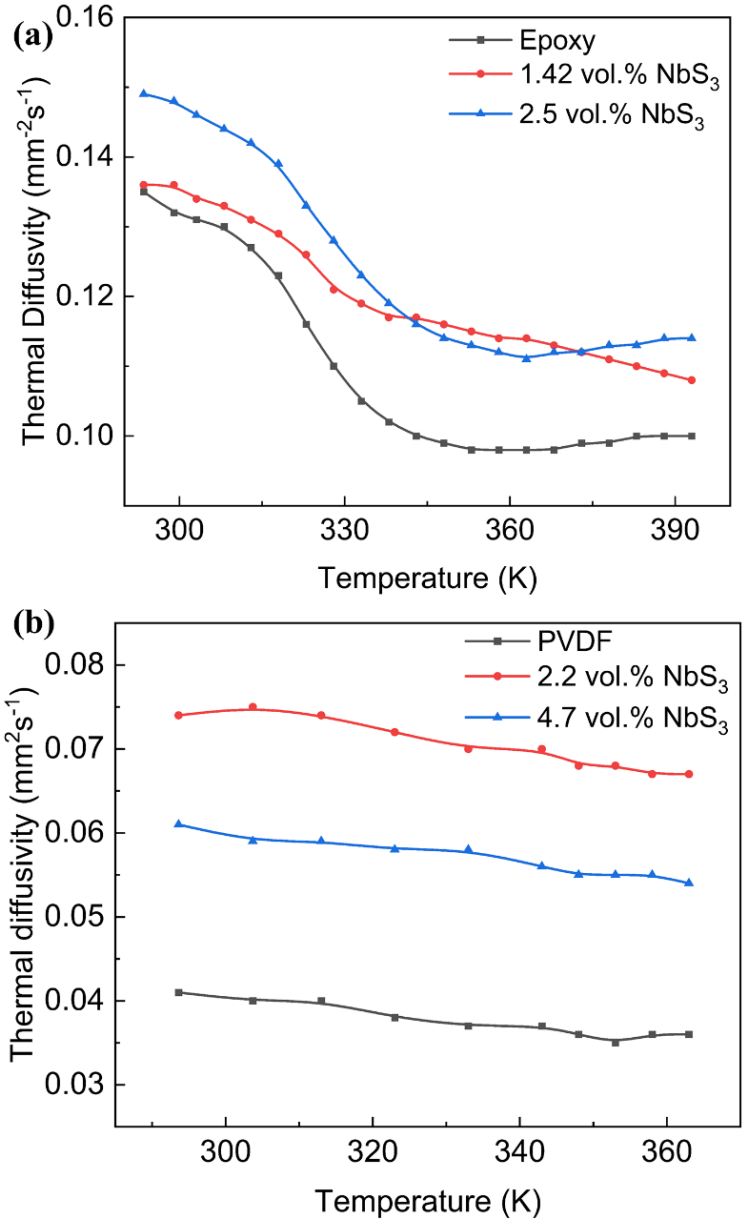

Fig. 3.5: Thermal diffusivity (a) pristine epoxy and two samples with NbS_3 fillers and (b) pristine PVDF and two samples with NbS_3 fillers.

The specific heat capacity values are extracted by using the LFA Analysis software. The heat capacity plots for both epoxy and PVDF composites determined could be seen in Fig. 3.6.

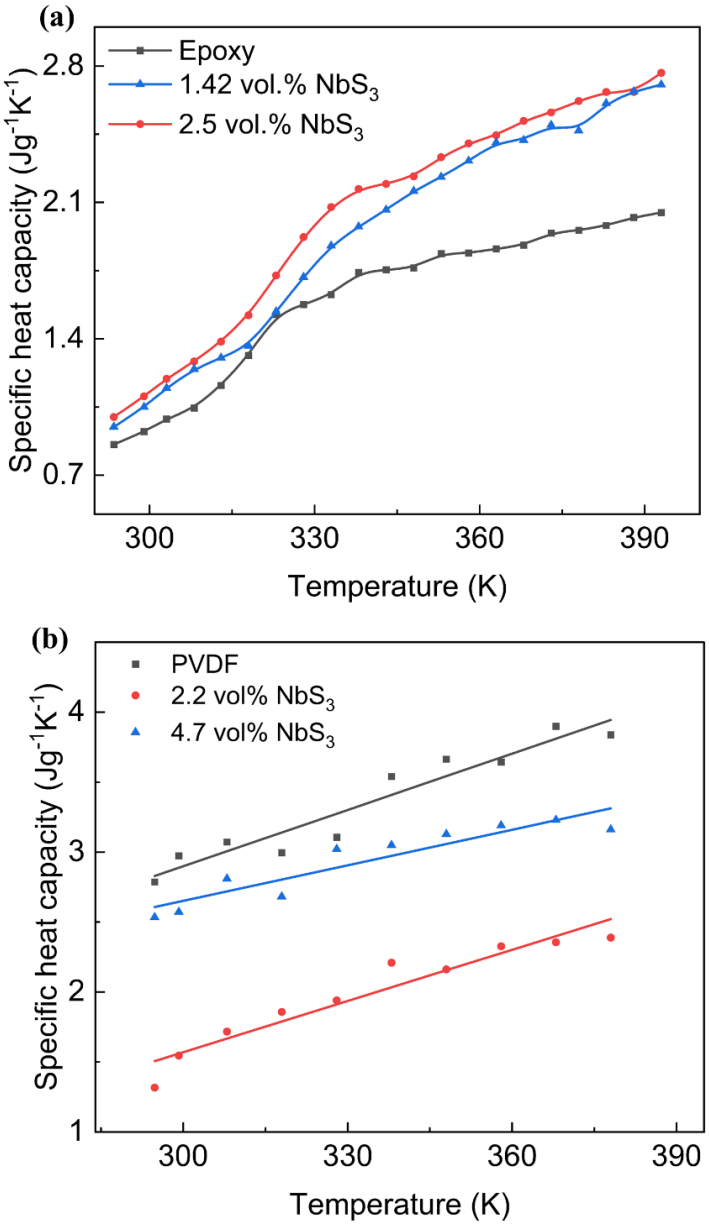

Fig. 3.6: Specific heat capacity (a) pristine epoxy and two samples with NbS_3 fillers and (b) pristine PVDF and two samples with NbS_3 fillers.

The thermal conductivity values are extracted by using Eq. 3.2. The thermal conductivity plots for both epoxy and PVDF composites determined could be seen in Fig. 3.7.

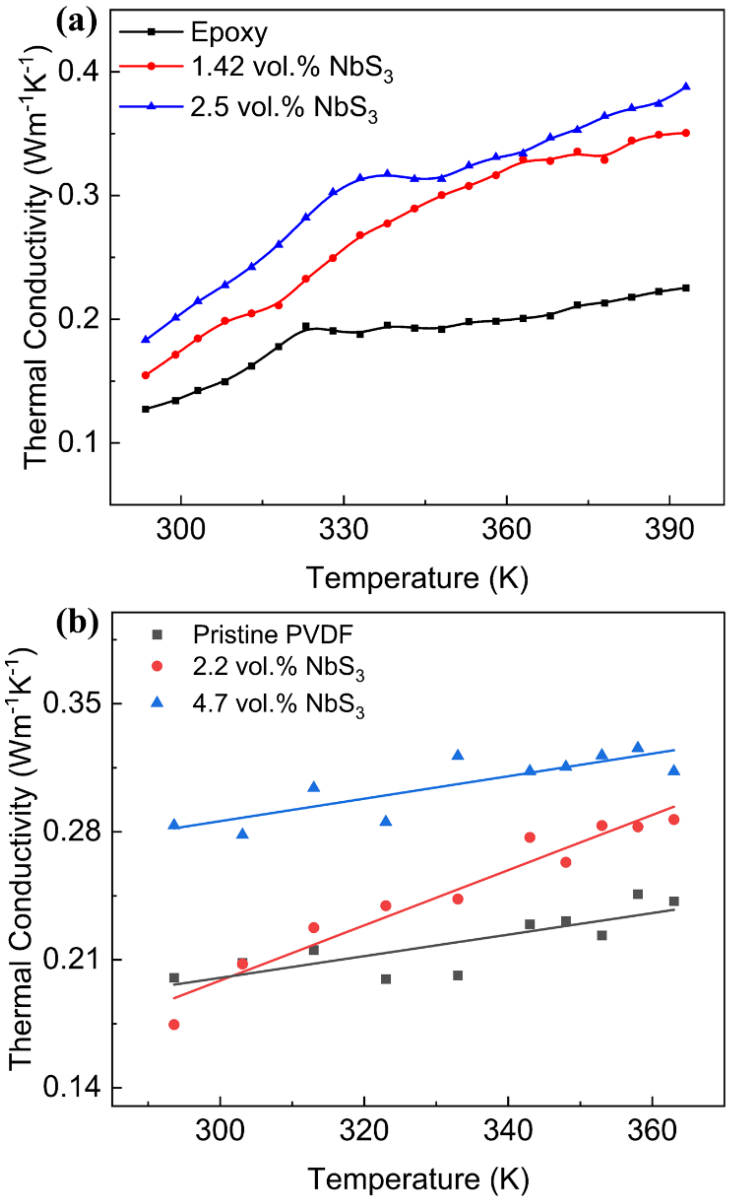

Fig. 3.7: Thermal conductivity (a) pristine epoxy and two samples with NbS_3 fillers and (b) pristine PVDF and two samples with NbS_3 fillers.

3.3 Raman Spectroscopy Characterization

Raman spectroscopy is another characterization method that provides chemical and structural information based on the scattering spectra from the material when the laser light passed. Raman spectroscopy detects photons caused by inelastic scattering, causing an increase or decrease in the energy of the molecule, unlike Rayleigh scattering which does not change the energy of the molecule, and this effect is called Raman scattering. The vibrational energy modes of the material could be determined by this process. It could also be used to differentiate the several polymorphs of the single material itself. Fig. 3.8 shows the image Raman instrument used in this work.

Fig. 3.8: Renishaw Raman system used in this project.

The different polymorphs of NbS_3 material were analyzed in this work. And able to find the spectral differences between NbS_3 Polymorph V from other NbS_3 Polymorphs

such as IV and VI. The polymorphs IV and VI exhibit some common peaks at ~145, ~155, ~189, ~ 250, and ~335 cm^{-1}, which has been reported that the Raman shift for NbS_3 – V is quite different from the other polymorphs as shown in Fig. 3.9 [61].

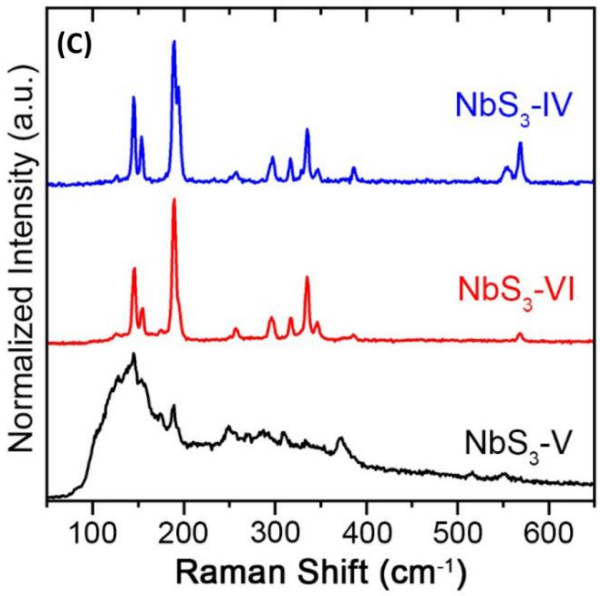

Fig. 3.9: Raman spectra of NbS_3 Polymorphs IV, V, and VI. NbS_3 IV and VI exhibits similar Raman shifts, whereas NbS_3 V shows quite a difference in the shifts and intensity. Reproduced from [62] Matthew A. Bloodgood, Yassamin Ghafouri, Pingrong Wei, and Tina T. Salguero, "Impact of the chemical vapor transport agent on polymorphism in the quasi-1D NbS_3 system", Appl. Phy. Lett. 120, 173103 (2022).

The NbS_3 nanowire is successfully exfoliated by the mechanical exfoliation process from the bulk-grown crystal. Now, the nanowire over the Si substrate is measured using Raman Spectroscopy. A single nanowire was chosen for the measurement. This nanowire is subjected to measurements at three different angles at 0^o, $45^{o,}$ and 90^o, based on the chain axis (c-axis), with the incident light, polarized in the x-direction. The results showed that the nanowire retained most of the peaks at all angles. The Raman shifts include 149 cm^{-1},

201 cm^{-1}, 254 cm^{-1}, 347 cm^{-1}, and 387 cm^{-1}. The two peaks that predominantly belong to NbS_3 V are at ~515 and ~ 555 cm^{-1}. Interestingly, the peak at ~555 cm^{-1} is not visible at 0° and as we measured at 45°, the peak signal sightly emerges with less intensity observed.

Finally, as the nanowire is turned to 90°, the peak was visible and confirms the polymorph V type. The peak at ~515 cm^{-1} is shaded along with the Silicon peak which is at 520 cm^{-1} as shown in Fig. 3.10. There is a new peak that emerged at 484 cm^{-1} in 90°. There is no clear evidence of this peak in the previous literature. The peak might be emerged due to the orientation, mixed phases, or mechanical cleavage in the sample preparation [62].

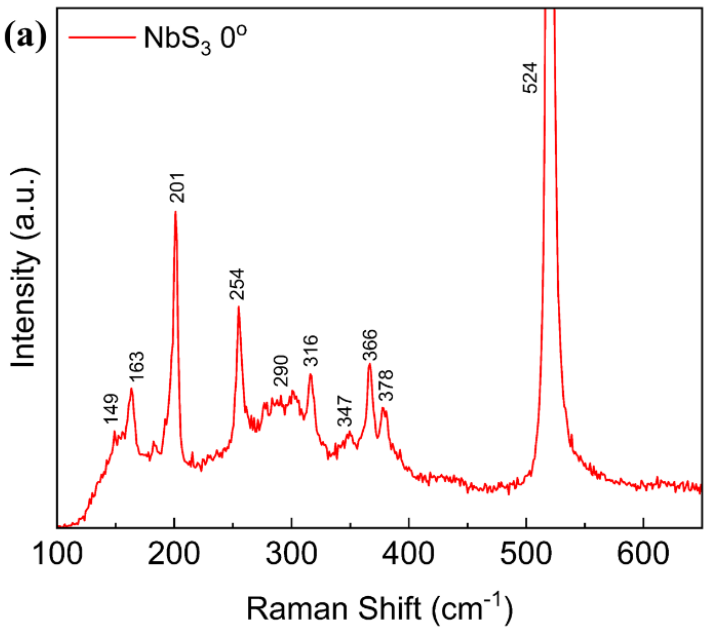

Fig. 3.10 (a): Raman spectrum of NbS_3 – V at 0° angle denoting the c-axis of the nanowire parallel with incident light polarized at x-direction.

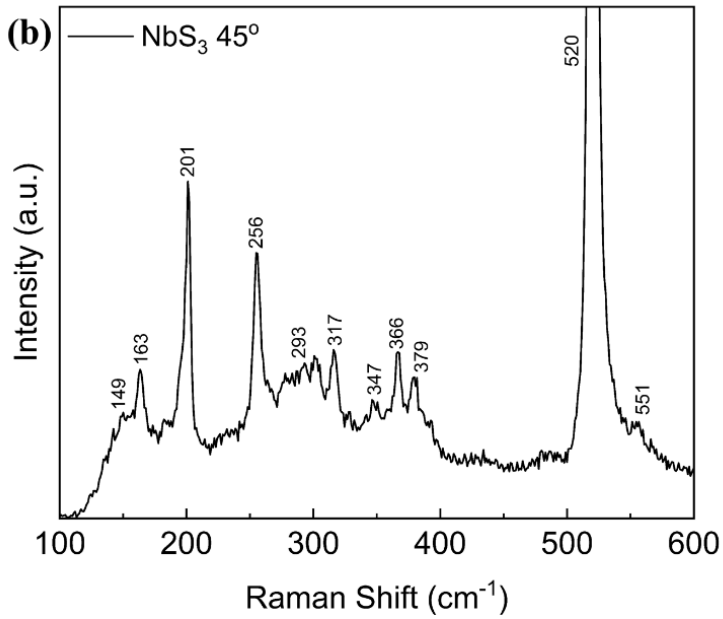

Fig. 3.10 (b): Raman spectrum of NbS_3 – V with c-axis at 45°, respective to incident light polarized at x-direction, consisting of every peak from 0° with a weak additional peak seen at 551 cm^{-1}.

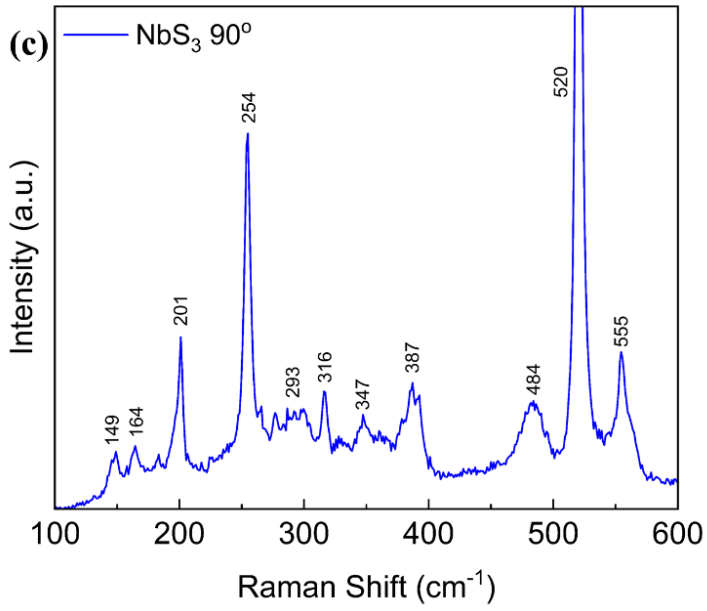

Fig. 3.10 (c): Raman spectrum of NbS_3 – V at 90° angle denoting the c-axis of the nanowire perpendicular with incident light polarized at x-direction, with two additional peaks noticed at 484 cm^{-1} and 555 cm^{-1}.

Now, the same procedure is repeated for the exfoliated NbS_3 filler. The spectra at both 0^o and 90^o are retained when compared to the NbS_3 crystal as shown in Fig. 3.11. This shows that the fillers are free from solvents and impurities after liquid phase exfoliation.

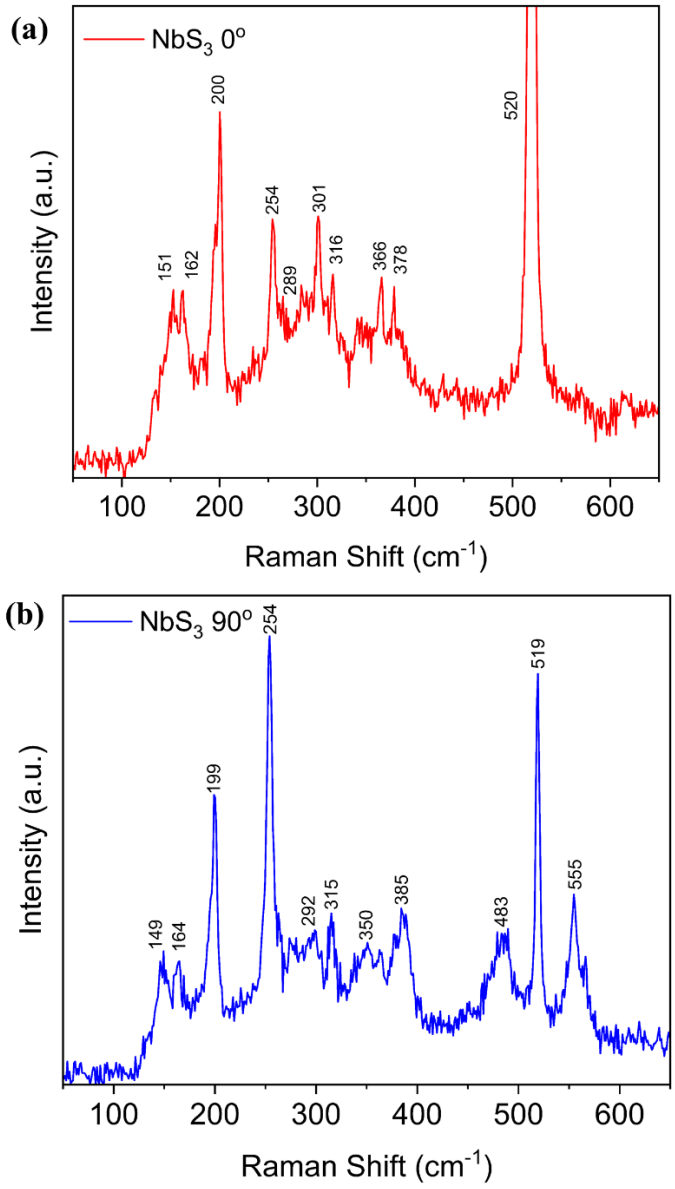

Fig. 3.11 (a, b): Raman spectrum of exfoliated NbS_3 fillers at two different angles 0^o and 90^o, with additional peaks seen at 483 cm^{-1} and 555 cm^{-1} similar to the bulk crystal at 90^o.

Chapter 4 Future Work

4.1. Preparation of the Ink

The preparation of inks has similarities with polymer inks, as ink itself is a composite made by mixing filler materials with solvents. The understanding of polymer composites leads to a possible realm of printed electronics with inks. In this work, the inks were made by liquid phase exfoliation (LPE). This solution-based synthesis method is simple and low-cost when compared to conventional methods of device fabrication. Thickness variation and high defect density of nanomaterials are inevitable in this employed method [63]. Mechanical exfoliation of the nanomaterial using Scotch tape is the most conventional method, which leads to variable thickness and hinders the scale-up of the production of the electronic device [64–66]. The expensive, high energy demand, and high temperature and high-pressure dependent conditions are required for Chemical vapor deposition (CVD), however, highly crystalline material can be synthesized.

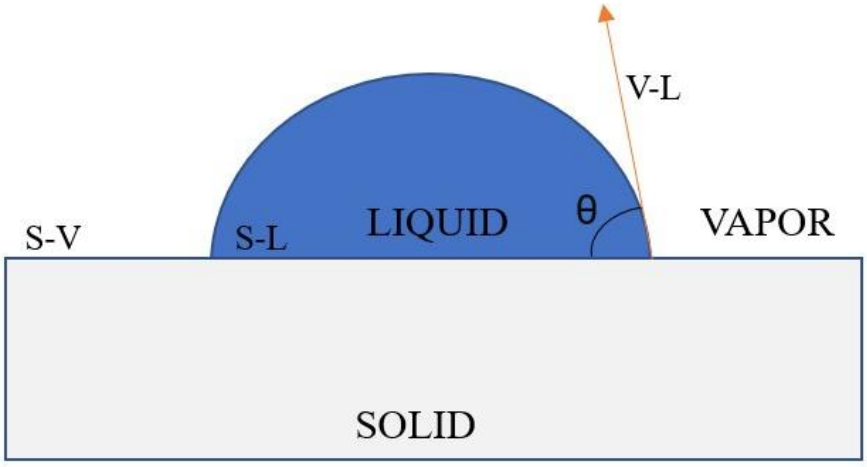

Fig. 4.1: Schematic of a droplet on a solid surface.

The ink during the printing process must be ideally spread over the surface and wet. For this to happen, the contact angle must be less than 90^{o} for good wetting of the surfaces. A good wetting will be achieved, if the solid interfacial surface tension should be greater than the ink, usually in the range of ~7 to ~10 mN m^{-1}. And contact angle between the droplet and the printing surface, defines the wettability of the ink, by using Young's equation. It is given by

$$\zeta_{sv} = \zeta_{sl} + \zeta_{lv}.\cos\theta \tag{2.1}$$

where ζ_{sv}, ζ_{lv}, and ζ_{sl} are the surface tensions of the solid surface, liquid surface, and solid-liquid interface, respectively [67].

The thermophysical behavior of the ink is determined by the disposal of ink droplets from the nozzle continuously without the formation of secondary droplets. The viscosity of the ink must be taken into the account, as highly viscous ink has high spreading capability and forms semi-circle geometries, this exhibits coffee-ring patterns resulting in undesired morphology [68].

$$Z = \frac{1}{Oh} = \frac{\sqrt{\zeta \rho a}}{\eta} \tag{2.2}$$

where η is the viscosity of the ink, a is the diameter of the nozzle, and ρ and ζ are the density and surface tension of the ink, respectively. Z value less than 1 leads to the formation of elongated droplets or no ink droplet formation at all. If the z value is higher than 14, there is a high possibility of satellite droplet formation. The optimum value of Z should lie between 1 to 14 [69–71].

The solution-based synthesis of nanomaterials contains two different approaches such as top-down and bottom-up. Liquid Phase Exfoliation, a top-down method is widely used for the preparation of functional inks. Solvents like dimethylformamide (DMF), N-methyl-2pyrroliodne (NMP), acetone, and ethanol have been employed for exfoliating 2D and 1D materials [72–75]. In this method, ethanol has been used as a solvent for exfoliation. To achieve an optimum Z-number between 1 to 14, a highly viscous solvent when compared to ethanol must be taken. So, ethylene glycol has been chosen as a secondary solvent. The Marangoni effect takes place due to the surface tension gradient caused by the difference in temperature or composition. Other than viscosity, the formation of the coffee ring is also suppressed because of the Marangoni effect [71].

Among the various developed contact and non-contact printing methods. Inkjet printing is one of the most promising approaches for large-are fabrication of flexible electronics. Printing of a wide collection of electronic components such as field-effect transistors, capacitors, photovoltaic devices, and light-emitting diodes has been demonstrated [27,76–79] The smaller number of process steps for producing devices, makes this method well-suited for mass production. The application of printed devices can be found in various areas such as wearable electronics, flexible radio frequency tags, organic light-emitting diodes, and organic solar cells [79–82]. The preparation and printing of the inks are discussed further.

4.2 Preparation of Device Contacts and Development of Electrode Pattern

The Si wafers are taken as substrate material for printing in this method. The cleaning of diced wafers should be done using ethanol sonication for 5 minutes, followed by drying with high-purity nitrogen gas. The spin coating method is used to coat the substrate with polymethyl methacrylate (PPMA). The substrate is placed inside the holder disk in the spin coater machine, and a few drops of PMMA are dropped on top of the wafer. The spin coater is programmed with a recipe for this process, it contains three steps: spreading, spinning, and stopping. After spin coating, the PMMA resist is heated above its glass transition temperature (T_g). The substrate is kept at 185 ℃ for two minutes after each layer of resistance is applied to the surface. The T_g for PMMA is between 100 ℃ and 160 ℃.

Table 4.1: Steps involved in spin coating

Steps	**Speed (rpm)**	**Duration (s)**	**Ramp rate (rpm/s)**
Step 1	400	3	400
Step 2	4000	45	2000
Step 3	0	2	2000

The electrodes were designed using DesignCAD software and were imported to Electron Beam Lithography (EBL) system, equipped with Leo SUPRA 55. In this process,

the electron beams were employed to write patterns on PMMA resist. The beams are steered by magnetic deflectors based on the computer-assisted design (CAD) pattern. The stage is moved for the CAD pattern by the stage controller [83,84].

A small dot of the diluted silver pattern is placed on the substrate surface to determine where the pattern should be written under the scanning electron microscope. To complete the EBL process, the PMMA resist is developed in a developer solution consisting of a mixture of methyl isobutyl ketone (MIBK) and isopropyl alcohol (IPA), at a ratio of 3:1. The sample is submerged in the solution for 20 s and then removed from the solution. It is then soaked in IPA for another 20 s, followed by drying with high-purity nitrogen gas.

4.3 Metallization and Lift-Off

Titanium (Ti) and Gold (Au) were used to deposit the metal electrodes on the substrate. The thickness ratio for Ti and Au is 1 to 10. Titanium is deposited first because it has good adhesion properties to the silicon wafer. It also assists in the better attachment of gold to the substrate. The samples are placed inside the electron beam evaporator chamber. The chamber pressure is pumped down to the pressure of 2×10^{-6} torr which is ideal for metal deposition. The deposition of different metal layers on the substrate is shown in Table 4.2.

Before the samples can be removed, the chamber is allowed to cool down in a vacuum after the deposition is done. Temescal Model BJD – 1800 electron beam evaporator is used, in this study. After the metallization step, the lift-off procedure is followed, where the pattern-less metalized part is removed using acetone. Also, it must be noted that if the thickness difference between the PMMA ad the deposited metal is large, then the sample must be soaked in acetone to lift off the unwanted metal from the surface. It would be difficult to remove the excess metal from the surface once the sample is taken out from the acetone. Finally, the pattern is verified using an optical microscope.

Table 4.2: Deposition rate of metal layers

Layers	**Metal**	**Deposition Rate (Å/s)**
Layer 1	Titanium (Ti)	0.5
Layer 2	Gold (Au)	0.5 (First 10 nm of the layer)
Layer 3	Gold (Au)	2

4.4 Thermophysical Properties and Printing Parameters of the Ink

During printing, there will be a high chance of non-uniform deposition of the material resulting in the “coffee-ring” effect. This could be avoided by adjusting the concentration of the materials used in making the ink.

The droplet formation behavior is characterized by the dimensionless number, $Z = \sqrt{\zeta \rho a}/\mu$, where a is the printer's nozzle diameter (m), ζ is the surface tension (N m^{-1}), ρ is the density (kg m^{-3}), and μ is the dynamic viscosity (Pa $\times$ s) of the ink, respectively [85]. The value of the Z-number must lie between the range of $1 \leq Z \leq 14$ for proper droplet formation. If the $Z > 14$, then there will be satellite droplet formation and formation of elongated ligaments if $Z < 1$. The Z-number influences the accuracy of the printing by depositing the ink in the desired areas [86,87]. The image of the 3D printer that could be used to print the ink on the substrate is shown in Fig. 4.2.

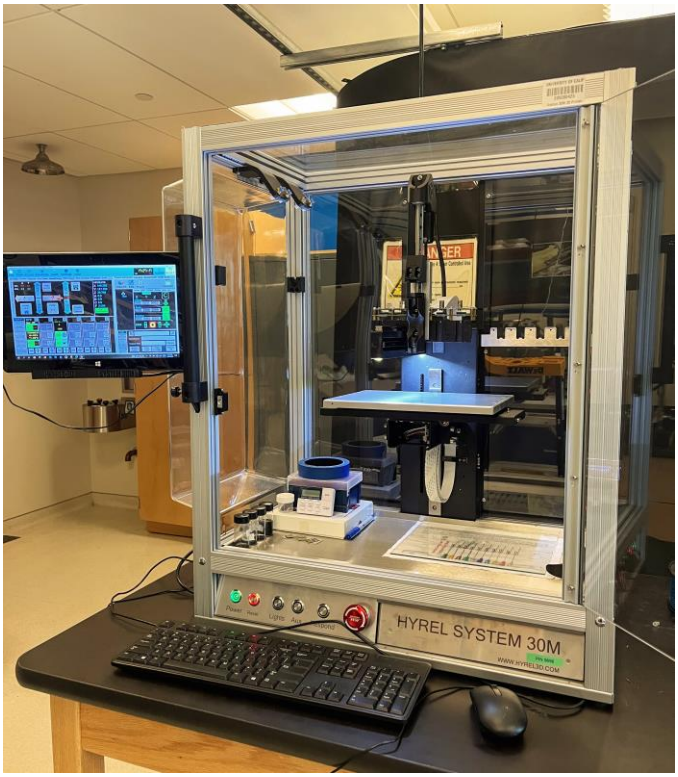

Fig. 4.2: Hyrel System 30M - 3D printer

Chapter 5 Conclusions

This thesis reports on the synthesis of polymer composites with fillers comprised of low-dimensional van der Waals materials. The quasi-one-dimensional (1D) van der Waals materials are characterized by the 1D motifs in their crystal structure. The research was focused on NbS_3 – a material that can form numerous polytypes. The fillers for the composites were prepared by the liquid-phase exfoliation of the small crystals into needle-like ribbons with nm-scale thickness and μm-scale length. The exfoliated NbS_3 fillers were dispersed in the solvents to produce composites. The speed mixing and sonication processes were used to control the filler sizes. The resulting composite materials were characterized using Raman light-scattering spectroscopy, differential scanning calorimetry, thermal diffusivity, and thermal conductivity measurements. The characterization data indicate that the NbS_3 fillers preserved their intrinsic properties. The results of the thesis research confirm that low-dimensional van der Waals materials are suitable for composite preparation. The obtained results can be used for the development of inks for printed electronics and multi-functional composites.

References

1. Dahiya, A.S.; Shakthivel, D.; Kumaresan, Y.; Zumeit, A.; Christou, A.; Dahiya, R. High-Performance Printed Electronics Based on Inorganic Semiconducting Nano to Chip Scale Structures. *Nano Converg* 2020, *7*, 33.

2. Dahiya, R.; Yogeswaran, N.; Liu, F.; Manjakkal, L.; Burdet, E.; Hayward, V.; Jorntell, H. Large-Area Soft e-Skin: The Challenges Beyond Sensor Designs. *Proceedings of the IEEE* 2019, *107*, 2016–2033.

3. García Núñez, C.; Liu, F.; Navaraj, W.T.; Christou, A.; Shakthivel, D.; Dahiya, R. Heterogeneous Integration of Contact-Printed Semiconductor Nanowires for High-Performance Devices on Large Areas. *Microsyst Nanoeng* 2018, *4*, 22.

4. Khan, S.; Lorenzelli, L.; Dahiya, R.S. Technologies for Printing Sensors and Electronics Over Large Flexible Substrates: A Review. *IEEE Sens J* 2015, *15*, 3164–3185.

5. Wu, W. Inorganic Nanomaterials for Printed Electronics: A Review. *Nanoscale* 2017, *9*, 7342–7372.

6. Rowley-Neale, S.J.; Foster, C.W.; Smith, G.C.; Brownson, D.A.C.; Banks, C.E. Mass-Producible 2D-MoSe $_2$ Bulk Modified Screen-Printed Electrodes Provide Significant Electrocatalytic Performances towards the Hydrogen Evolution Reaction. *Sustain Energy Fuels* 2017, *1*, 74–83.

7. Hu, G.; Yang, L.; Yang, Z.; Wang, Y.; Jin, X.; Dai, J.; Wu, Q.; Liu, S.; Zhu, X.; Wang, X.; et al. A General Ink Formulation of 2D Crystals for Wafer-Scale Inkjet Printing. *Sci Adv* 2020, *6*.

8. Schulte, K.; Gojny, F.H.; Fiedler, B.; Sandler, J.K.W.; Bauhofer, W. Carbon Nanotube-Reinforced Polymers: A State of the Art Review. In *Polymer Composites*; Springer-Verlag: New York; 3–23.

9. R, Lokesh.; V, Jagadesh.; S, Suresh. Mechanical and Low Velocity Impact Behavior of Al Based Kevlar Fabric Reinforced Epoxy Laminate. *International Journal of Applied Engineering Research* 2021, *16*, 660–669.

10. Haupert, F.; Wetzel, B. Reinforcement of Thermosetting Polymers by the Incorporation of Micro- and Nanoparticles. In *Polymer Composites*; Springer-Verlag: New York; 45–62.

11. Sreekala, M.S.; Eger, C. Property Improvements of an Epoxy Resin by Nanosilica Particle Reinforcement. In *Polymer Composites*; Springer-Verlag: New York; 91–105.

12. Malkapuram, R.; Kumar, V.; Negi, Y.S. Recent Development in Natural Fiber Reinforced Polypropylene Composites. *Journal of Reinforced Plastics and Composites* 2009, *28*, 1169–1189.

13. Rahman, A.; Ali, I.; al Zahrani, S.M.; Eleithy, R.H. A Review of the Applications of Nanocarbon Polymer Composites. *Nano* 2011, *06*, 185–203.

14. Schelling, P.K.; Shi, L.; Goodson, K.E. Managing Heat for Electronics. *Materials Today* 2005, *8*, 30–35.

15. Park, W.; Guo, Y.; Li, X.; Hu, J.; Liu, L.; Ruan, X.; Chen, Y.P. High-Performance Thermal Interface Material Based on Few-Layer Graphene Composite. *The Journal of Physical Chemistry C* 2015, *119*, 26753–26759.

16. Shahil, K.M.F.; Balandin, A.A. Graphene–Multilayer Graphene Nanocomposites as Highly Efficient Thermal Interface Materials. *Nano Lett* 2012, *12*, 861–867.

17. Han, X. Ductile van Der Waals Materials. *Science (1979)* 2020, *369*, 509–509.

18. Asensio, M.C.; Batzill, M. Interfaces and Heterostructures of van Der Waals Materials. *Journal of Physics: Condensed Matter* 2016, *28*, 490301.

19. Liu, Y.; Weiss, N.O.; Duan, X.; Cheng, H.-C.; Huang, Y.; Duan, X. Van Der Waals Heterostructures and Devices. *Nat Rev Mater* 2016, *1*, 16042.

20. Li, J.; Naiini, M.M.; Vaziri, S.; Lemme, M.C.; Östling, M. Inkjet Printing of MoS_2. *Adv Funct Mater* 2014, *24*, 6524–6531.

21. Cho, B.; Yoon, J.; Lim, S.K.; Kim, A.R.; Kim, D.-H.; Park, S.-G.; Kwon, J.-D.; Lee, Y.-J.; Lee, K.-H.; Lee, B.H.; et al. Chemical Sensing of 2D Graphene/MoS_2 Heterostructure Device. *ACS Appl Mater Interfaces* 2015, *7*, 16775–16780.

22. Kelly, A.G.; Hallam, T.; Backes, C.; Harvey, A.; Esmaeily, A.S.; Godwin, I.; Coelho, J.; Nicolosi, V.; Lauth, J.; Kulkarni, A.; et al. All-Printed Thin-Film Transistors from Networks of Liquid-Exfoliated Nanosheets. *Science (1979)* 2017, *356*, 69–73.

23. Baraghani, S.; Abourahma, J.; Barani, Z.; Mohammadzadeh, A.; Sudhindra, S.; Lipatov, A.; Sinitskii, A.; Kargar, F.; Balandin, A.A. Printed Electronic Devices with Inks of TiS_3 Quasi-One-Dimensional van Der Waals Material. *ACS Appl Mater Interfaces* 2021, *13*, 47033–47042.

24. Tortorich, R.; Choi, J.-W. Inkjet Printing of Carbon Nanotubes. *Nanomaterials* 2013, *3*, 453–468.

25. Song, J.-W.; Kim, J.; Yoon, Y.-H.; Choi, B.-S.; Kim, J.-H.; Han, C.-S. Inkjet Printing of Single-Walled Carbon Nanotubes and Electrical Characterization of the Line Pattern. *Nanotechnology* 2008, *19*, 095702.

26. Fan, Z.; Wei, T.; Luo, G.; Wei, F. Fabrication and Characterization of Multi-Walled Carbon Nanotubes-Based Ink. *J Mater Sci* 2005, *40*, 5075–5077.

27. Han, S.-Y.; Lee, D.-H.; Herman, G.S.; Chang, C.-H. Inkjet-Printed High Mobility Transparent–Oxide Semiconductors. *Journal of Display Technology* 2009, *5*, 520–524.

28. Dasgupta, S.; Kruk, R.; Mechau, N.; Hahn, H. Inkjet Printed, High Mobility Inorganic-Oxide Field Effect Transistors Processed at Room Temperature. *ACS Nano* 2011, *5*, 9628–9638.

29. Randle, M.D.; Lipatov, A.; Mansaray, I.; Han, J.E.; Sinitskii, A.; Bird, J.P. Collective States and Charge Density Waves in the Group IV Transition Metal Trichalcogenides. *Appl Phys Lett* 2021, *118*, 210502.

30. Island, J.O.; Molina-Mendoza, A.J.; Barawi, M.; Biele, R.; Flores, E.; Clamagirand, J.M.; Ares, J.R.; Sánchez, C.; van der Zant, H.S.J.; D'Agosta, R.; et al. Electronics and Optoelectronics of Quasi-1D Layered Transition Metal Trichalcogenides. *2D Mater* 2017, *4*, 022003.

31. Stolyarov, M.A.; Liu, G.; Bloodgood, M.A.; Aytan, E.; Jiang, C.; Samnakay, R.; Salguero, T.T.; Nika, D.L.; Rumyantsev, S.L.; Shur, M.S.; et al. Breakdown Current Density in H-BN-Capped Quasi-1D $TaSe_3$ Metallic Nanowires: Prospects of Interconnect Applications. *Nanoscale* 2016, *8*, 15774–15782.

32. Abdulsalam, M.; Joubert, D.P. Structural and Electronic Properties of MX_3 (M = Ti, Zr and Hf; X = S, Se, Te) from First Principles Calculations. *Eur Phys J B* 2015, *88*, 177.

33. Island, J.O.; Biele, R.; Barawi, M.; Clamagirand, J.M.; Ares, J.R.; Sánchez, C.; van der Zant, H.S.J.; Ferrer, I.J.; D'Agosta, R.; Castellanos-Gomez, A. Titanium Trisulfide (TiS_3): A 2D Semiconductor with Quasi-1D Optical and Electronic Properties. *Sci Rep* 2016, *6*, 22214.

34. Muratov, D.S.; Vanyushin, V.O.; Vorobeva, N.S.; Jukova, P.; Lipatov, A.; Kolesnikov, E.A.; Karpenkov, D.; Kuznetsov, D. v.; Sinitskii, A. Synthesis and Exfoliation of Quasi-1D $(Zr,Ti)S_3$ Solid Solutions for Device Measurements. *J Alloys Compd* 2020, *815*, 152316.

35. Zybtsev, S.G.; Pokrovskii, V.Ya.; Nasretdinova, V.F.; Zaitsev-Zotov, S. V.; Pavlovskiy, V. v.; Odobesco, A.B.; Pai, W.W.; Chu, M.-W.; Lin, Y.G.; Zupanič, E.; et al. NbS_3: A Unique Quasi-One-Dimensional Conductor with Three Charge Density Wave Transitions. *Phys Rev B* 2017, *95*, 035110.

36. Geremew, A.; Bloodgood, M.A.; Aytan, E.; Woo, B.W.K.; Corber, S.R.; Liu, G.; Bozhilov, K.; Salguero, T.T.; Rumyantsev, S.; Rao, M.P.; et al. Current Carrying

Capacity of Quasi-1D $ZrTe_3$ Van Der Waals Nanoribbons. *IEEE Electron Device Letters* 2018, *39*, 735–738.

37. Lipatov, A.; Wilson, P.M.; Shekhirev, M.; Teeter, J.D.; Netusil, R.; Sinitskii, A. Few-Layered Titanium Trisulfide (TiS_3) Field-Effect Transistors. *Nanoscale* 2015, *7*, 12291–12296.

38. Bigg, D.M.; Stutz, D.E. Plastic Composites for Electromagnetic Interference Shielding Applications. *Polym Compos* 1983, *4*, 40–46.

39. Pan, Y.; Weng, G.J.; Meguid, S.A.; Bao, W.S.; Zhu, Z.-H.; Hamouda, A.M.S. Percolation Threshold and Electrical Conductivity of a Two-Phase Composite Containing Randomly Oriented Ellipsoidal Inclusions. *J Appl Phys* 2011, *110*, 123715.

40. Zybtsev, S.G.; Pokrovskii, V.Ya.; Nasretdinova, V.F.; Zaitsev-Zotov, S.V. Growth, Crystal Structure and Transport Properties of Quasi One-Dimensional Conductors NbS_3. *Physica B Condens Matter* 2012, *407*, 1696–1699.

41. Kargar, F.; Barani, Z.; Salgado, R.; Debnath, B.; Lewis, J.S.; Aytan, E.; Lake, R.K.; Balandin, A.A. Thermal Percolation Threshold and Thermal Properties of Composites with High Loading of Graphene and Boron Nitride Fillers. *ACS Appl Mater Interfaces* 2018, *10*, 37555–37565.

42. Ladani, R.B.; Bhasin, M.; Wu, S.; Ravindran, A.R.; Ghorbani, K.; Zhang, J.; Kinloch, A.J.; Mouritz, A.P.; Wang, C.H. Fracture and Fatigue Behaviour of Epoxy Nanocomposites Containing 1-D and 2-D Nanoscale Carbon Fillers. *Eng Fract Mech* 2018, *203*, 102–114.

43. Feng, L.; Zheng, J.; Yang, H.; Guo, Y.; Li, W.; Li, X. Preparation and Characterization of Polyethylene Glycol/Active Carbon Composites as Shape-Stabilized Phase Change Materials. *Solar Energy Materials and Solar Cells* 2011, *95*, 644–650.

44. Cavallaro, G.; de Lisi, R.; Lazzara, G.; Milioto, S. Polyethylene Glycol/Clay Nanotubes Composites. *J Therm Anal Calorim* 2013, *112*, 383–389.

45. Wang, S.; Xie, G.; Su, Y.; Su, L.; Zhang, Q.; Du, H.; Tai, H.; Jiang, Y. Reduced Graphene Oxide-Polyethylene Oxide Composite Films for Humidity Sensing via Quartz Crystal Microbalance. *Sens Actuators B Chem* 2018, *255*, 2203–2210.

46. Awasthi, K.; Awasthi, S.; Srivastava, A.; Kamalakaran, R.; Talapatra, S.; Ajayan, P.M.; Srivastava, O.N. Synthesis and Characterization of Carbon Nanotube–Polyethylene Oxide Composites. *Nanotechnology* 2006, *17*, 5417–5422.

47. Song, Y.S. Rheological Characterization of Carbon Nanotubes/Poly(Ethylene Oxide) Composites. *Rheol Acta* 2006, *46*, 231–238.

48. Aslam, M.; Kalyar, M.A.; Raza, Z.A. Polyvinyl Alcohol: A Review of Research Status and Use of Polyvinyl Alcohol Based Nanocomposites. *Polym Eng Sci* 2018, *58*, 2119–2132.

49. Banitaba, S.N.; Semnani, D.; Heydari-Soureshjani, E.; Rezaei, B.; Ensafi, A.A. Nanofibrous Poly(Ethylene Oxide)-based Structures Incorporated with Multi-walled Carbon Nanotube and Graphene Oxide as All-solid-state Electrolytes for Lithium Ion Batteries. *Polym Int* 2019, *68*, 1787–1794.

50. Praveena, S.D.; Ravindrachary, V.; Bhajantri, R.F.; Ismayil Free Volume-Related Microstructural Properties of Lithium Perchlorate/Sodium Alginate Polymer Composites. *Polym Compos* 2014, *35*, 1267–1274.

51. Khan, A.F.; Brownson, D.A.C.; Foster, C.W.; Smith, G.C.; Banks, C.E. Surfactant Exfoliated 2D Hexagonal Boron Nitride (2D-HBN) Explored as a Potential Electrochemical Sensor for Dopamine: Surfactants Significantly Influence Sensor Capabilities. *Analyst* 2017, *142*, 1756–1764.

52. Rao, V.J.; Qi, H.; Berger, F.J.; Grieger, S.; Kaiser, U.; Backes, C.; Zaumseil, J. Liquid Phase Exfoliation of Rubrene Single Crystals into Nanorods and Nanobelts. *ACS Nano* 2021, *15*, 20466–20477.

53. Fan, P.; Wang, L.; Yang, J.; Chen, F.; Zhong, M. Graphene/Poly(Vinylidene Fluoride) Composites with High Dielectric Constant and Low Percolation Threshold. *Nanotechnology* 2012, *23*, 365702.

54. Eswaraiah, V.; Sankaranarayanan, V.; Ramaprabhu, S. Inorganic Nanotubes Reinforced Polyvinylidene Fluoride Composites as Low-Cost Electromagnetic Interference Shielding Materials. *Nanoscale Res Lett* 2011, *6*, 137.

55. Xu, X.; Yang, C.; Yang, J.; Huang, T.; Zhang, N.; Wang, Y.; Zhou, Z. Excellent Dielectric Properties of Poly(Vinylidene Fluoride) Composites Based on Partially Reduced Graphene Oxide. *Compos B Eng* 2017, *109*, 91–100.

56. Specific Heat Capacity. *Netzsch.* https://analyzing-testing.netzsch.com/en-US/training-know-how/glossary/specific-heat-capacity-cp/.

57. *Thermal Analysis of Polymers*; Menczel, J.D., Prime, R.B., Eds.; John Wiley & Sons, Inc.: Hoboken, NJ, USA, 2009; ISBN 9780470423837.

58. Mettler Toledo. Thermal Analysis UserCom 11 [Brochure].

59. O'Neill, M.J. Measurement of Specific Heat Functions by Differential Scanning Calorimetry. *Anal Chem* 1966, *38*, 1331–1336.

60. Nunes dos Santos, W.; Mummery, P.; Wallwork, A. Thermal Diffusivity of Polymers by the Laser Flash Technique. *Polym Test* 2005, *24*, 628–634.

61. Bloodgood, M.A.; Wei, P.; Aytan, E.; Bozhilov, K.N.; Balandin, A.A.; Salguero, T.T. Monoclinic Structures of Niobium Trisulfide. *APL Mater* 2018, *6*, 026602.

62. Bloodgood, M.A.; Ghafouri, Y.; Wei, P.; Salguero, T.T. Impact of the Chemical Vapor Transport Agent on Polymorphism in the Quasi-1D NbS_3 System. *Appl Phys Lett* 2022, *120*, 173103.

63. Gao, X.; Bian, G.; Zhu, J. Electronics from Solution-Processed 2D Semiconductors. *J Mater Chem C Mater* 2019, *7*, 12835–12861.

64. Desai, S.B.; Madhvapathy, S.R.; Amani, M.; Kiriya, D.; Hettick, M.; Tosun, M.; Zhou, Y.; Dubey, M.; Ager, J.W.; Chrzan, D.; et al. Gold-Mediated Exfoliation of Ultralarge Optoelectronically-Perfect Monolayers. *Advanced Materials* 2016, *28*, 4053–4058.

65. Pető, J.; Ollár, T.; Vancsó, P.; Popov, Z.I.; Magda, G.Z.; Dobrik, G.; Hwang, C.; Sorokin, P.B.; Tapasztó, L. Spontaneous Doping of the Basal Plane of MoS_2 Single Layers through Oxygen Substitution under Ambient Conditions. *Nat Chem* 2018, *10*, 1246–1251.

66. Radisavljevic, B.; Radenovic, A.; Brivio, J.; Giacometti, V.; Kis, A. Single-Layer MoS_2 Transistors. *Nat Nanotechnol* 2011, *6*, 147–150.

67. Zisman, W.A. Relation of the Equilibrium Contact Angle to Liquid and Solid Constitution. In; 1964; 1–51.

68. Hu, G.; Kang, J.; Ng, L.W.T.; Zhu, X.; Howe, R.C.T.; Jones, C.G.; Hersam, M.C.; Hasan, T. Functional Inks and Printing of Two-Dimensional Materials. *Chem Soc Rev* 2018, *47*, 3265–3300.

69. Jang, D.; Kim, D.; Moon, J. Influence of Fluid Physical Properties on Ink-Jet Printability. *Langmuir* 2009, *25*, 2629–2635.

70. Derby, B. Inkjet Printing of Functional and Structural Materials: Fluid Property Requirements, Feature Stability, and Resolution. *Annu Rev Mater Res* 2010, *40*, 395–414.

71. Hu, G.; Albrow-Owen, T.; Jin, X.; Ali, A.; Hu, Y.; Howe, R.C.T.; Shehzad, K.; Yang, Z.; Zhu, X.; Woodward, R.I.; et al. Black Phosphorus Ink Formulation for Inkjet Printing of Optoelectronics and Photonics. *Nat Commun* 2017, *8*, 278.

72. Kang, J.; Sangwan, V.K.; Wood, J.D.; Hersam, M.C. Solution-Based Processing of Monodisperse Two-Dimensional Nanomaterials. *Acc Chem Res* 2017, *50*, 943–951.

73. Backes, C.; Higgins, T.M.; Kelly, A.; Boland, C.; Harvey, A.; Hanlon, D.; Coleman, J.N. Guidelines for Exfoliation, Characterization and Processing of Layered Materials Produced by Liquid Exfoliation. *Chemistry of Materials* 2017, *29*, 243–255.

74. Barani, Z.; Kargar, F.; Ghafouri, Y.; Ghosh, S.; Godziszewski, K.; Baraghani, S.; Yashchyshyn, Y.; Cywiński, G.; Rumyantsev, S.; Salguero, T.T.; et al. Electrically Insulating Flexible Films with Quasi-1D van Der Waals Fillers as Efficient Electromagnetic Shields in the GHz and Sub-THz Frequency Bands. *Advanced Materials* 2021, *33*, 2007286.

75. Nicolosi, V.; Chhowalla, M.; Kanatzidis, M.G.; Strano, M.S.; Coleman, J.N. Liquid Exfoliation of Layered Materials. *Science (1979)* 2013, *340*.

76. Fu, Y.; Zhang, P.; Li, B.; Zhang, B.; Yu, Y.; Shen, Z.; Zhang, X.; Wu, J.; Nan, C.; Zhang, S. Inkjet Printing of Perovskite Nanosheets for Microcapacitors. *Adv Electron Mater* 2021, *7*, 2100402.

77. Conti, S.; Lai, S.; Cosseddu, P.; Bonfiglio, A. An Inkjet-Printed, Ultralow Voltage, Flexible Organic Field Effect Transistor. *Adv Mater Technol* 2017, *2*, 1600212.

78. Schackmar, F.; Eggers, H.; Frericks, M.; Richards, B.S.; Lemmer, U.; Hernandez-Sosa, G.; Paetzold, U.W. Perovskite Solar Cells with All-Inkjet-Printed Absorber and Charge Transport Layers. *Adv Mater Technol* 2021, *6*, 2000271.

79. Park, S.-I.; Xiong, Y.; Kim, R.-H.; Elvikis, P.; Meitl, M.; Kim, D.-H.; Wu, J.; Yoon, J.; Yu, C.-J.; Liu, Z.; et al. Printed Assemblies of Inorganic Light-Emitting Diodes for Deformable and Semitransparent Displays. *Science (1979)* 2009, *325*, 977–981.

80. Bidoki, S.; McGorman, D.; Lewis, D.; Clark, M.; Horler, G.; Miles, R.E. Inkjet Printing of Conductive Patterns on Textile Fabrics. *AATCC Rev* 2005, *5*, 11–14.

81. Redinger, D.; Molesa, S.; Yin, S.; Farschi, R.; Subramanian, V. An Ink-Jet-Deposited Passive Component Process for RFID. *IEEE Trans Electron Devices* 2004, *51*, 1978–1983.

82. Ganesan, S.; Mehta, S.; Gupta, D. Fully Printed Organic Solar Cells – a Review of Techniques, Challenges and Their Solutions. *Opto-Electronics Review* 2019, *27*, 298–320.

83. Rai-Choudhury, P. *Handbook of Microlithography, Micromachining, and Microfabrication. Volume 1: Microlithography*; SPIE PRESS, 1997; ISBN 9781510607965.

84. Tseng, A.A.; Kuan Chen; Chen, C.D.; Ma, K.J. Electron Beam Lithography in Nanoscale Fabrication: Recent Development. *IEEE Transactions on Electronics Packaging Manufacturing* 2003, *26*, 141–149.

85. Fromm, J.E. Numerical Calculation of the Fluid Dynamics of Drop-on-Demand Jets. *IBM J Res Dev* 1984, *28*, 322–333.

86. Torrisi, F.; Hasan, T.; Wu, W.; Sun, Z.; Lombardo, A.; Kulmala, T.S.; Hsieh, G.-W.; Jung, S.; Bonaccorso, F.; Paul, P.J.; et al. Inkjet-Printed Graphene Electronics. *ACS Nano* 2012, *6*, 2992–3006.

87. Jang, D.; Kim, D.; Moon, J. Influence of Fluid Physical Properties on Ink-Jet Printability. *Langmuir* 2009, *25*, 2629–2635.